Accepted manuscript – Final publication in Acta Materialia, (2021)

Disordered interfaces enable high temperature thermal stability and strength in a nanocrystalline aluminum alloy

Glenn H. Balbus[a], Johann Kappacher[b], David J. Sprouster[c], Fulin Wang[a], Jungho Shin[a], Yolita M. Eggeler[d], Timothy J. Rupert[e], Jason R. Trelewicz[c,f], Daniel Kiener[g], Verena Maier-Kiener[b], Daniel S. Gianola[a*]

[a]*Materials Department, University of California, Santa Barbara, CA 93106, USA*
[b]*Department of Materials Science, Chair of Physical Metallurgy & Metallic Materials, Montanuniversität Leoben, Franz Josef-Str. 18, Leoben A-8700, Austria*
[c]*Department of Materials Science and Chemical Engineering, Stony Brook University, Stony Brook, NY 11794, USA*
[d]*Laboratory for Electron Microscopy, Karlsruhe Institute of Technology, Karlsruhe D-76131, Germany*
[e]*Department of Materials Science and Engineering, University of California, Irvine, CA 92697, USA*
[f]*Institute for Advanced Computational Science, Stony Brook University, Stony Brook, NY 11794, USA*
[g]*Department of Materials Science, Chair of Materials Physics, Montanuniversität Leoben, Jahnstr. 12, Leoben A-8700, Austria*
*Corresponding author.
E-mail address: gianola@ucsb.edu (D.S. Gianola)

Abstract: Lightweighting of structural materials has proven indispensable in the energy economy, predicated on alloy design with high strength-to-weight ratios. Modern aluminum alloys have made great strides in ambient temperature performance and are amenable to advanced manufacturing routes such as additive manufacturing, but lack elevated temperature robustness where gains in efficiency can be obtained. Here, we demonstrate the intentional design of disorder at interfaces, a notion generally associated with thermal runaway in traditional materials, in a segregation-engineered ternary nanocrystalline Al-Ni-Ce alloy that exhibits exceptional thermal stability and elevated temperature strength. *In-situ* transmission electron microscopy in concert with ultrafast calorimetry and X-ray total scattering point to synergistic co-segregation of Ce and Ni driving the evolution of amorphous intergranular films separating sub-10 nm Al-rich grains, which gives rise to emergent thermal stability. We ascribe this intriguing behavior to near-equilibrium interface conditions followed by kinetically sluggish intermetallic precipitation in the confined disordered region. The resulting outstanding mechanical performance at high homologous temperatures lends credence to the efficacy of promoting disorder in alloy design and discovery.

Keywords: Grain boundaries; Nanocrystalline metals; Amorphous intergranular films; Thermal stability

© 2021. This manuscript version is made available under the CC-BY-NC-ND 4.0 license
http://creativecommons.org/licenses/by-nc-nd/4.0/
Published version accessible at: https://doi.org/10.1016/j.actamat.2021.116973

1. Introduction

Materials processing strategies to imbue ambient or low temperature strength to metallic alloys, specifically those that induce grain refinement, often come at the expense of high temperature performance, owing to the introduction of copious non-equilibrium defects such as grain boundaries that render the material unstable. This tradeoff is emblematic in nanocrystalline and amorphous alloys, which exhibit desirable low temperature mechanical properties but are hindered by grain growth [1] and crystallization [2], [3] at moderate temperatures causing the properties of interest to vanish. These instabilities have stimulated research efforts investigating the role of chemistry [4] and processing [5] to mitigate these issues in both classes of materials; their commonality arises from structural disorder at the abundant interfaces in nanocrystals and throughout the bulk in amorphous materials, suggesting that the lack of thermal stability may be intrinsically linked to atomic-scale topological disorder.

The predominance of microstructural runaway in nanocrystalline metals has stimulated recent efforts to mitigate grain growth via binary alloy design that employs thermodynamic and kinetic strategies for endowing interfaces with thermal stability. Thermodynamic stabilization hinges on the reduction in grain boundary energy through the addition of elements with a favorable enthalpy of segregation [6], [7], whereas kinetic stabilization occurs in systems that exhibit the formation of subtle atomic clusters that pin the grain boundary, reducing the boundary velocity [8]–[11]. Both frameworks emphasize chemical segregation to grain boundaries and are theoretically and practically beneficial for imparting microstructural stability in nanocrystalline metals. Compared to many pure nanocrystalline metals, which exhibit grain growth below 30 % of their melting point [1], [12], [13], these alloying strategies have resulted in the creation of several alloys which exhibit microstructural stability at temperatures above 45% of their melting point [4], [9], [10], [14]–[19], owing to the careful selection of alloying additions.

Despite these successes, demanding applications require structural materials that possess the room temperature strength of nanocrystalline alloys, allow for operation at increasingly high temperatures, and circumvent the limited damage tolerance associated with solute segregation at ordered grain boundaries [20], [21]. For instance, current lightweight aluminum alloys utilized in the transportation sector are plagued by their poor strength retention at service temperatures [22], motivating the recent development of aluminum alloys with better thermal stability [23]–[26]. The application of interface-aware alloying to stabilize a nanocrystalline aluminum microstructure to enable high specific strengths (strength-to-weight ratio) over a wide range of service temperatures has received little attention, despite unprecedented potential gains in energy efficiency [27].

In a recent strategy that runs counter to the conventional wisdom that disorder is anathema to thermal stability, nanocrystalline alloys containing amorphous intergranular films (AIFs) have surprisingly exhibited exceptional thermal stability, retaining their nanocrystalline microstructures after long durations at temperatures near their melting point [18], [28], [29], indicative of the most promising thermal stability exhibited by a nanocrystalline metal to date. While many studies have focused on binary alloys, specifically Cu-Zr base alloys, expansion into multicomponent alloying [30] has demonstrated that higher order alloying strategies may further enhance these desirable properties. Moreover, the presence of AIFs in Cu-Zr alloys gives rise to remarkable damage tolerance and ductility without compromising room temperature strength [31], [32].

Here, we extend this principle to a lightweight Al-alloy intentionally alloyed with Ni and Ce based on their proclivity to: co-segregate, satisfy glass formability criteria, and exhibit structurally disordered interfaces which impart outstanding high temperature stability and strength. We present a detailed study using ultrafast calorimetry, in-situ transmission electron microscopy (TEM) heating, X-ray total scattering, and high temperature nanoindentation to uncover the link between the structural evolution of the fully continuous AIFs and thermal stability. Exposure to intermediate temperatures drives chemical segregation and structural evolution of AIFs in the nanocrystalline Al-Ni-Ce alloy, enhancing the mechanical properties and delaying precipitation of intermetallic phases to higher temperatures. This collective behavior renders the microstructure stable above 64% of its melting point and sustains the ultrahigh mechanical strength intrinsic to nanocrystalline materials to high homologous temperatures.

2. Materials and methods

Nanocrystalline Al-Ni-Ce samples were synthesized using an AJA ATC 1800 sputter deposition system as described in Ref. [28]. The alloy composition was controlled using confocal DC sputtering from two, 2-inch diameter sputter targets, of pure Al (99.999% purity) and pre-alloyed $Al_{87}Ni_7Ce_6$ (at. %, 99.95% purity) from Angstrom Sciences. Sputtering was performed using a power of 100 W for the pure Al target and 175 W for the alloyed target, resulting in a net deposition rate of 0.27 nm s^{-1}. Base pressures prior to each deposition were below 10^{-7} Torr. All depositions were performed using a processing chamber pressure of 3 mTorr Ti-gettered Ar. To promote a nanocrystalline microstructure, the targets were shuttered every 36 s for 5 s. 1 μm thick samples were deposited on Si (100) wafers for mechanical testing, onto soda lime glass wafers for X-ray studies, and on single crystal NaCl wafers for ultrafast calorimetry. Electron transparent (40 nm) samples were deposited onto Cu transmission electron microscopy (TEM) grids with C support films for scanning transmission electron microscopy (STEM) analysis, as well as onto Protochips Fusion E-chip heating devices with C support films for in-situ STEM heating. All STEM experiments were performed using a Thermo Fisher Talos G2 200X STEM operating at 200 kV. Grain size measurements were performed using dark field TEM images with a small objective aperture placed over the $\{111\}$ and $\{200\}$ diffraction rings. At least 70 grains were measured from each condition investigated.

Ex-situ annealing studies were performed to set temperatures of 200 °C, 325 °C, and 380 °C under vacuum (10^{-7} Torr) in the AJA sputter deposition chamber. A heating ramp rate of 0.1 °C s^{-1} was used to reach the desired temperature, followed by 1 h holds at each set temperature. The heater was then shut off and the system allowed to cool slowly under vacuum over the course of 2-3 h.

Samples deposited on NaCl wafers were submerged in steam distilled water to dissolve the NaCl wafer and produce freestanding 1 μm thick films. These were then dried in a desiccator overnight and cut into ≈ 400 μm × 400 μm area pieces and manipulated onto a Mettler Toledo UFS Flash Differential Scanning Calorimetry (DSC) chip using a single hair brush. Silicone oil was used as a thermal contact for all data presented here. Samples were heated from 25 °C to 425 °C and then cooled back to 25 °C at heating rates between 100 and 5000 °C s^{-1}. As the samples were manually cut to size, and each experiment was a new sample, the masses of all heating runs were slightly different. To account for this difference, all heat flow plots have been normalized by the magnitude of the precipitation peak for straightforward comparison.

In-situ TEM heating experiments were performed at a constant heating and cooling rate of 0.5 °C s^{-1}. Samples were heated to a set temperature, held at temperature for ≈ 2 min, and subsequently cooled while acquiring bright field (BF), annular dark field (ADF) and high angle annular dark field (HAADF) STEM images. Before and after each heating segment, selected area diffraction patterns (SADPs), energy dispersive X-ray spectroscopy (EDS) spectra, and conventional dark field (DF) TEM images were recorded. Set-point temperatures of 100 °C, 200 °C, 325 °C, and 380 - 450 °C were chosen in order to compare with *ex-situ* heating experiments. This interrupted heating profile enabled the acquisition of multiple datasets during evolution of the microstructure to provide insight into both the structural and chemical evolution of the system. The dwell time during the heating segments was calibrated such that each image was acquired over 0.5 s. EDS spectral maps of 1000 X 1000 pixels were collected at room temperature by summing at least 60 individual spectral images collected with a 4 µs dwell time per pixel. HAADF-STEM images were simultaneously acquired with EDS spectral maps. Chemical profiles were generated using Velox (Thermo Fisher Scientific). For the as-deposited and 325 °C EDS maps, the data was rebinned to 250 X 250 pixels (4x reduction) using HyperSpy [33]. The pixel-wise EDS spectra were summed in order to generate spectra with sufficient intensity for accurate elemental quantification within each rebinned pixel. Diffraction patterns of the α-$Al_{11}Ce_3$ [011] zone axis were simulated using EMsoft [34] and crystal structures of α-$Al_{11}Ce_3$ and Al_3Ni were obtained from The Materials Project [35].

In order to study the anticipated segregation behavior of the Ni and Ce in an Al matrix, and the corresponding effects on the Al-Ni-Ce alloy, modified nanocrystalline Monte Carlo (NCMC) simulations[36]–[40] were performed on bi-crystal geometries. As discussed extensively in [36]–[38], these simulations employ the use of a large lattice, divided into grains with a unique grain ID, effectively a modified Ising model. Unique bond energies are used to differentiate the interactions between each chemical species either within the grain interior or at a grain boundary. These simulations do not incorporate the amorphous structure of the grain boundaries, nor additional complexity such as grain boundary character dependence, but are useful in interpreting one aspect of the chemical segregation observed experimentally. At each step in the simulation, two atoms of different chemical species are selected at random, swapped, and the total energy of the system is recalculated. The swaps are accepted according to a conventional Metropolis algorithm. Grain boundary swaps were not incorporated in these simulations in order to preserve the bi-crystal. A simulation cell with dimensions 20 X 20 X 5 (FCC unit cells) with a planar grain boundary in the $+$y direction was utilized. The cell was randomly decorated with Ni and Ce solute atoms in order to achieve the desired bulk composition. Two binary compositions, $\mathrm{Al_{98}Ce_2}$ and $\mathrm{Al_{98}Ni_2}$, and one ternary composition, $\mathrm{Al_{97}Ni_2Ce_1}$ were investigated. The grain boundary geometry was fixed and periodic boundary conditions were used, effectively creating a layered structure with two grain boundaries. The system was then equilibrated at several temperatures over $>$ 6,000,000 Monte Carlo steps.

Thin film pair distribution function (PDF) measurements [41] were performed at the National Synchrotron Light Source-II, using beamline 28-ID1 [42]. All measurements were performed in transmission geometry with an amorphous silicon-based flat panel detector (PerkinElmer) mounted orthogonal to the beam path and centered on the beam. The sample-to-detector distances and tilts of the detector relative to the beam were refined using a Nickel powder standard. The wavelength of the incident X-rays was 0.1666 Å (74.42 keV). 80 diffraction patterns, all exhibiting identical scattering, were collected for each sample and the two-dimensional images were then averaged together and radially integrated, to obtain the one-dimensional diffraction patterns. The scattering component from the glass substrate was subtracted from the diffraction patterns. The diffraction patterns collected were corrected for PDF-specific corrections (self-absorption, multiple scattering and Compton scattering) and converted to atomic PDFs, G(r), over a Q-range of 1-20 $\mathrm{Å^{-1}}$.

Elevated temperature nanoindentation experiments were performed on 1 μm thick samples deposited onto Si using a Nanomechanics InSEM Nanoindenter equipped with a 50 mN load cell. Hardness measurements were performed with a diamond Berkovich tip indenter manufactured by Synton-MDP at an indentation strain rate of 0.1 $\mathrm{s^{-1}}$. The tip area function was calibrated on fused silica before all experiments [43]. Each data point was acquired from a unique sample which was heated from room temperature to the specific testing temperature at 10 °C $\mathrm{min^{-1}}$, held at temperature for 2 h to minimize temperature gradients prior to indentation, tested for $\approx$ 1.5 h, and then cooled to room temperature at 10 °C $\mathrm{min^{-1}}$. No systematic variation in strength was observed during the 1.5 h test time. The reported hardness values were averaged between 180 and 220 nm indentation depth. The depth selected for hardness measurements was chosen to optimize between minimal substrate influence, and sufficient penetration to minimize geometrical inaccuracies, instabilities and transient behavior of the testing platform.

3. Results and discussion

3.1 Elucidation of thermal stability in nanocrystalline Al-Ni-Ce

Our alloy design strategy is premised on the use of chemical complexity and the propensity of multiple interface-segregating species in a multicomponent alloy system [30]. We selected the Al-Ni-Ce ternary system owing to the synergistic co-segregating tendencies of Ni and Ce [28], which will be discussed in greater detail in Section 3.2, and the resulting chemical and structural grain boundary configuration that satisfies the classical criteria for glass formability [44] and AIF formation [29]. We first examine the evolution of the microstructure and its role in the thermal stability of nanocrystalline Al-Ni-Ce. *Ex-situ* annealing experiments performed at 200 °C - 380 °C (0.5 - 0.7 T_m), (Figure 1a-d) indicate that the sputter deposited Al-Ni-Ce alloy does not exhibit grain growth at temperatures of ≈ 325 °C (0.64 T_m) for one h. High angle annular dark field (HAADF) images recorded using identical image acquisition parameters in Figure 1b,c suggest that grain boundary regions are enriched in Ni and Ce at temperatures between 200 °C - 325 °C, consistent with chemical partitioning in devitrified Al-Ni-Ce alloys [45]. The contrast present in the as-deposited state is primarily diffraction contrast [28]. After annealing at 380 °C, the intermetallic phases Al_3Ni and $Al_{11}Ce_3$ precipitate (Figure 1d) and the remaining Al microstructure coarsens significantly. To compare the thermal stability of the nanocrystalline Al-Ni-Ce alloy to other nanocrystalline alloys, we define a grain size retention (GSR) metric as follows:

$$GSR = \frac{d_0}{d_i} \tag{1}$$

where d_0 is the average initial grain size of the material and d_i is the average grain size after some thermal exposure. GSR is defined such that a microstructure that does not exhibit grain growth attains a value of 1, and microstructures that coarsen decrease from 1 to 0. Figure 1e presents the GSR extracted from samples presented in Figure 1a-d alongside several thermally stable nanocrystalline alloys from the literature [9], [12], [13], [15]–[18], demonstrating the remarkable stability of the Al-Ni-Ce alloy. The full grain size distributions (Figure 2) exhibit a narrow spread that does not markedly evolve during annealing prior to intermetallic precipitation. Abnormal grain growth, which has been reported in nanocrystalline alloy systems containing heterogeneous grain boundary segregation [46], can thus be eliminated as a potential instability mechanism. Literature data for various other nanocrystalline alloys was taken from the shortest exposures reported, although some instances of longer exposures (i.e. Ni-18W, W-20Ti, Cu-10Ta) are included as well.

The alloys included in Figure 1e are representative of several classes of nanocrystalline alloys: pure metals, "stable" alloys, and amorphous intergranular film (AIF)-containing alloys. Pure metals exhibit the least resistance to coarsening, experiencing significant grain growth at 0.2 - 0.3 T_m. "Thermally stable" alloys exhibit markedly higher thermal stability, pushing up to 0.4 - 0.5 T_m prior to significant coarsening. These alloys include the highest performing nanocrystalline alloys to-date, including W-Ti [4], Cu-Ta [9], [10], and Ni-W [15]. At the highest homologous temperatures are AIF-containing alloys, specifically a Cu-Zr nanocrystalline alloy and the Al-Ni-Ce alloy [18], [31]. These AIF containing alloys exhibit the highest thermal stability of a nanocrystalline metal to date.

The thermal envelope of microstructural stability and underlying thermal signatures associated with chemical redistribution and intermetallic precipitation were quantified using ultrafast differential scanning calorimetry (DSC). Heat flow traces (Figure 3a) demonstrate the presence of two exothermic events, labeled T_{gb} and T_{precip}. The event labeled as T_{gb} occurs at temperatures that coincide with chemical enrichment of grain boundaries in Ni and Ce (Figure 1b,c), while the second exothermic event (T_{precip}) occurs at temperatures above 325 °C and is ascribed to the nucleation and growth of intermetallics ($\mathrm{Al}_{11}\mathrm{Ce}_3$ and $\mathrm{Al}_3\mathrm{Ni}$). Qualitatively, the heat flow traces in Figure 3a indicate that the precipitation event (T_{precip}) is not strongly dependent upon heating rate, unlike the low temperature exothermic event (T_{gb}). Kissinger analysis (Figure 3b) suggests activation energies of 116 kJ/mol and 413 kJ/mol for the exothermic events at T_{gb} and T_{precip}, respectively. The onset temperature of the grain boundary exothermic event was used for this analysis, as the peaks are not well defined for all heating rates. The choice of using either the onset or peak temperature for the precipitation event does not significantly alter the deduced activation energies. The activation energy of 116 kJ/mol is consistent with diffusive activity of Al, Ni, or Ce in an FCC-Al matrix [47], [48], whereas the precipitation activation energy (413 kJ/mol) is uncharacteristically large. Typical values for intermetallic precipitation in Al-Ni-Ce glasses are ≈ 200 kJ/mol [49], less than half the value we measure. The precipitation activation energy we measure is also larger than those in all ternary amorphous Al-transition metal-rare earth alloys [49], [50] and is comparable to higher order amorphous Al-alloys such as AlNiYCoLa [51], whose large activation energy originates in the formation and evolution of several intermetallics with multiple crystal structures.

In-situ TEM heating experiments (Figure 4 and Supplementary Videos) provide direct visualization of the structural evolution during thermal exposure of the Al-Ni-Ce alloy. The evolution at temperatures below 325 °C is characterized by Ni and Ce grain boundary enrichment and subtle evolution of the Al grains. Individual heating segments to temperatures below 150 °C indicate little microstructural activity, consistent with the absence of thermal events in the calorimetric signal. At temperatures above 150 °C, instances of grain reorientation occur and become more numerous at temperatures approaching 325 °C (Figure 4a, b). The reorientation events are evident in the diffraction patterns, where more intense and discrete spots after annealing at 325 °C signify fewer unique grain orientations in the imaged area (Figure 4d). The presence of more intense diffraction spots often implies grain growth, however grain size distributions measured during the *in-situ* heating experiments (Figure 5) indicate no significant grain growth. After heating to 450 °C, the HAADF snapshots (Figure 4c) show significant grain growth alongside the nucleation of $\mathrm{Al}_{11}\mathrm{Ce}_3$ and $\mathrm{Al}_3\mathrm{Ni}$ precipitates (Figures 4d, B.3) during the second exothermic event detected in the heat flow trace (Figure 3b and 4e). The negligible mutual solubility of alloying additions in the intermetallic phases suggests that the chemical distribution prior to intermetallic precipitation - i.e., co-segregation and co-location of Ni and Ce to AIFs - severely hinders the subsequent precipitation kinetics. For instance, in order for $\mathrm{Al_{11}Ce_3}$ to precipitate, the initial Ni content within the AIF must diffuse away sufficiently in order for the local chemical environment to facilitate nucleation of $\mathrm{Al_{11}Ce_3}$ as there is limited solubility of Ni in $\mathrm{Al_{11}Ce_3}$ [52], [53]. Such behavior has been observed during controlled solidification of other Al-Ni-Rare Earth alloys [54]. Furthermore, the role of confinement in the form of both size effects, which suppress the crystallization of nanoscale amorphous alloys [55], and strain energy penalties associated with intermetallic precipitation within the sub-nm-scale AIFs [56] may complicate intermetallic precipitation in the Al-Ni-Ce alloy, giving rise to the high activation energy of precipitation. These observations, in conjunction with the calorimetric analysis, suggest a co-dependent thermal stability behavior wherein the presence of the AIF stabilizes the microstructure, and the subsequent AIF evolution limits the precipitation of $\mathrm{Al_{11}Ce_3}$ and $\mathrm{Al_3Ni}$ intermetallics, giving rise to the exceptional high temperature stability of the alloy.

3.2 Bi-crystal nanocrystalline Monte Carlo simulations

A 2D projection of the initialized structure for the ternary composition is shown in Figure 6a,b. In order to confirm equilibration of the system, the total energy of the system was computed at every successful atomic swap. The change in energy during simulations performed at several temperatures are shown in Figure 6c. The change in energy was calculated by subtracting the current system energy by the initial system energy. It appears that a local equilibrium condition sufficient for concluding the simulation is reached in all cases. The low temperature simulations exhibit significantly fewer successful swaps, as the system cannot access a more energetically-favorable condition by subsequent atomic swaps; the variability in the system energy diminishes significantly after several thousand successful swaps. These results, especially at low temperature, may be metastable equilibrium states. Nevertheless, the total reduction in energy for simulations performed at 0 K after $> 6{,}000{,}000$ total Monte Carlo steps is lower than those attained at elevated temperatures in all simulations presented in this study.

2D equilibrated snapshots, as well as grain boundary enrichment factor as a function of temperature are shown in Figure 7. Grain boundary enrichment factor (β) is the ratio of the local grain boundary composition (χ_a^{gb}) to the total concentration in the alloy (χ_a): $\beta = \frac{\chi_a^{gb}}{\chi_a}$. The bond energies used in these simulations, while approximations, are as follows: for like elements, the bond energies were estimated from the cohesive energy of the pure elements [57]; the pairwise bond energies between unlike elemental species were calculated using the mixing enthalpies of binary alloys [58]; the grain boundary bond energies for unlike elemental species were calculated using estimates of the segregation enthalpies from [6], [59], [60] and formulations presented in Ref. [61]. The enthalpies of segregation of Ce in Al reported in Ref. [59] are strongly negative, such that Ce exhibits a strong propensity for segregation away from Al, in good agreement with experimental evidence of Al-Ce alloys. As such, the simulation was performed with a large, negative enthalpy of segregation for Ce in Al of -20 kJ/mol, close to the combined elastic and chemical interactions presented in Ref. [59]. Ni, on the other hand, exhibits a slightly positive enthalpy of segregation in Al according to Refs. [6], [59], [60], so the small, positive value of 5 kJ/mol was used in the simulations. In the binary cases, this results in clear grain boundary enrichment of Ce, and grain boundary depletion of Ni, evident both in the 2D slices and in the grain boundary excess measurements. The pairwise interaction between Ni and Ce is attractive, so an enthalpy of segregation of Ni in Ce of -25 kJ/mol was used [59]. This value agrees with the experimentally observed segregation behavior and negative mixing enthalpies in amorphous alloys [45], [58]. These bond energies result in in Ce and Ni enrichment of grain boundaries in the ternary alloy at low temperatures. At high temperatures in the ternary alloy, the grain boundary enrichment of Ni decreases, but remains greater than 1 for all simulations performed, highlighting the import of ternary alloying in this system - the favorable interactions between Ni and Ce promotes grain boundary enrichment of Ni in the ternary case, as opposed to grain boundary depletion of Ni in the binary case. Lastly, the temperature at which Ce depletion begins is shifted to higher temperatures in the ternary case, further highlighting the importance of favorable Ni-Ce interactions.

3.3 Amorphous intergranular films underlie thermal stability

The structural evolution of the AIFs that occurs during annealing below 325 °C improves the low-temperature hardness of the alloy [28] while simultaneously impacting the phase decomposition, as evidenced by the high activation energy for intermetallic precipitation (Figure 3b). To elucidate the structural signatures underpinning the thermal stability, synchrotron X-ray scattering experiments were performed on the as-deposited and 200 °C annealed material. The total scattering patterns (Figure 8a, b), structure factor (Figure 8b), and resulting pair distribution function (PDF) analysis (Figure 8d) provide crucial insight on short- and medium-range ordering motifs through the detection of diffuse scattering signals that are usually overwhelmed by the Bragg scattering features. Specifically, the background subtracted total scattering intensity (Figure 8b) exhibits contributions from the amorphous phase (the AIFs) corresponding to the peaks near 1.5 and 2.6 $Å^{-1}$. These peaks become less prominent upon annealing, whereas crystalline features at 4.4 and 6.8 $Å^{-1}$ become more pronounced after annealing. As we do not observe significant grain growth or the nucleation of new grains in Figure 1b,c as well as in the *in-situ* TEM experiments (Figure 4a-c), nor in previous work [28], we ascribe this evolution in intensity primarily to the structural evolution within the AIF regions.

We further examine the evolution of the amorphous grain boundary regions using the total structure factor in Figure 8c, which was calculated directly from the background corrected XRD patterns using PDFGetX3 [62]. Two peaks in Figure 8c originate from the amorphous content of the material: the feature labeled 'Pre-peak' at 1.5 $Å^{-1}$ and another at 2.8 $Å^{-1}$. As the feature at 2.8 $Å^{-1}$ does not evolve significantly with annealing, we will focus our discussion on the feature at 1.5 $Å^{-1}$. Pre-peaks, subtle yet distinguishable features in diffraction experiments of amorphous materials [63], have been observed via neutron and X-ray diffraction experiments of many Al-based liquid and amorphous alloys [64], [65]. These features arise from the short- and medium-range order of solute additions, which take on a quasi-periodic arrangement due to strong pairwise atomic interactions and the packing motifs of polyhedral clusters [49], [64]–[66]. This ordering is manifested as a reduction in the pre-peak present in the structure factor (Figure 8c) of the nanocrystalline Al-Ni-Ce alloy after annealing, which is accompanied by a reduction in the correlation peaks associated with the disordered, amorphous structure below radial distances of 5 Åin the atomic PDF (Figure 8d). While understanding the chemical complexity from the PDF results is beyond the scope of this work since it requires dedicated modeling to deconvolute the contributions from the different bonding environments, we note here the mutual consistency in the structure factor and PDF and their agreement with the electron diffraction results. We observe a significant reduction in the pre-peak present in the structure factor (Figure 8c) of the nanocrystalline Al-Ni-Ce alloy after annealing. This reduction in pre-peak magnitude is indicative of a destabilization of the regular packing of solute-centered polyhedra within the AIFs, which has important implications for thermal stability. Structural rearrangements that reduce the connectivity of solute-centered atomic clusters giving rise to the pre-peak also effectively minimize structural precursors to the equilibrium crystalline phases, resulting in enhanced thermal stability [67], [68]. The structural evolution evident in Figure 8c occurs concomitantly with the chemical enrichment of the AIF in Ni and Ce, as evidenced in the EDS maps presented in Figure 9a,b (as well as Figures 1b,c, B.1, B.2). This increase in local Ni and Ce concentration from $Al_{94.6}Ni_{4.1}Ce_{1.3}$ to $Al_{86.6}Ni_{10}Ce_{3.4}$ inhibits the regular packing of solute-centered polyhedra, consistent with increasing thermal stability in amorphous alloys with increasing concentrations of Ni and Ce [67]. This is further manifested by the increased intensity and decreased breadth of the Bragg peaks, suggesting that any intragranular Ni and Ce has diffused towards the grain boundary. A schematic depiction of the hypothesized structural evolution of the AIF is shown in Figure 10a,b, where the solute centered polygons exhibit more edge-sharing in the as-deposited case and more vertex-sharing with higher Ni and Ce concentrations. The reduction in structural motifs that provide favorable templating with the equilibrium $Al_{11}Ce_3$ and Al_3Ni phase - as indicated by the reduction in the pre-peak intensity, the chemically challenging precipitation process, as well as potential strain energy penalties [56] and size effects [55], all underlie the microstructural stability of the Al-Ni-Ce alloy. Interestingly, the intrinsic stability owing to the formation of AIFs and its evolution to suppress precipitation act in a co-dependent way; the thermodynamic stabilization mechanism evidently begets the kinetic ones.

Our detailed thermal analysis and characterization of the Al-Ni-Ce samples collectively point to an emergent thermal stability. Annealing at temperatures below 325 °C induces three phenomena that occur in concert: 1) chemical enrichment of the amorphous grain boundaries in Ni and Ce, 2) Al grain reorientation, and 3) a reduction in the medium-range structural order of the AIFs. All three phenomena are fundamentally mediated by diffusive activities, in good agreement with the low temperature activation energy obtained from calorimetric analysis. The chemical enrichment of the grain boundaries, evident in the HAADF micrographs and EDS measurements, is consistent with previous investigations of amorphous alloys due to the negligible solubility of Ni and Ce in Al [45]. Grain reorientation occurs as a result of diffusive events [69], potentially minimizing the surface or grain boundary energy. The signatures from the X-ray total scattering analysis suggest the increase in Ni and Ce in the AIFs causes a destabilization of Ni- and Ce-centered, polyhedral, medium-range order in the amorphous regions of the material, complicating intermetallic precipitation. These concerted effects enhance the thermal stability of the microstructure by stabilizing the AIFs and concomitantly improve the mechanical properties and deformation behavior of the alloy [28].

3.4 Origin of elevated temperature strength

We next examine the influence of chemical and structural ordering within the AIF on the elevated temperature mechanical properties of nanocrystalline Al-Ni-Ce. The room and elevated temperature mechanical properties of the Al-Ni-Ce alloy measured by high temperature nanoindentation. These data were converted to strength values assuming a Tabor factor of 3 (i.e. $\sigma = \frac{H}{3}$) [70]–[72]. This Tabor factor is large given the high hardness to modulus ratio [73], resulting in lower reported strength values, but was used to account for any potential pressure sensitivity of the alloy [74]. Figure 11a presents an estimate of the room temperature specific strength of the Al-Ni-Ce alloy. The density was calculated using the composition of the alloy determined by STEM EDS ($Al_{94.9}Ni_{3.8}Ce_{1.3}$), and the elemental densities for constituent elemental metals. Figure 11a demonstrates the high strength, low density, and extremely small grain size of the Al-Ni-Ce alloy relative to many Al-based alloys. The properties of conventional Ti-6Al-4V, Mg AZ31B, and Al 6061-T6, all high specific strength alloys utilized in aerospace applications, are included here as well to demonstrate the exceptional properties of the Al-Ni-Ce alloy, and highlight the potential benefits of utilizing such an alloy in engineering applications.

The temperature-dependent properties (Figure 11b) of the as-deposited Al-Ni-Ce alloy demonstrate that while several nanostructured Al alloys exhibit comparable room temperature strength, our alloy exhibits higher strength at elevated temperatures compared to all previously reported nanostructured (nanotwinned) [75] and high performance conventional Al alloys [22]–[25]. The strength decreases from 1650 MPa at room temperature in the as-deposited state to 1350 MPa at 250 °C. After heating to 250 °C and cooling back down, the room temperature strength of the alloy attains a maximum of 1800 MPa, providing additional corroboration of a grain boundary relaxation process. The strength drops considerably at temperatures above 300 °C due to significant microstructural evolution and intermetallic precipitation, evident in the room temperature hardness measurements performed after heating (Figure 11b, hatched marker). At 325 °C the strength was measured to be 230 MPa - a large reduction relative to the room temperature performance of the alloy, but still considerably higher than many precipitation-strengthened Al-alloys, including high-performance Ce-containing cast Al-alloys [23], [25].

3.5 Activation parameter analysis

Despite these impressive elevated temperature mechanical properties, the mechanistic origin underpinning the temperature-dependent strength of the alloy is not obvious. While all metallic alloys exhibit temperature-dependent strength, we seek to unravel the competing roles of the amorphous and crystalline domains on this temperature dependence in our AIF-containing nanocrystalline alloy. Bulk amorphous metals exhibit a near universal temperature-dependent yield strength due to their shear transformation zone (STZ) based plasticity [76]. While such a model is inappropriate for describing the overall behavior of the Al-Ni-Ce alloy due to the large volume fraction of crystalline grains, the temperature dependence predicted by this model is quite similar, suggestive of a similar underlying deformation process.

One promising attribute of elevated temperature indentation testing is the ability to derive activation parameters from both the rate and temperature sensitivity of the measured properties, which provide insight into the mechanistic underpinning of the mechanical behavior. Several analysis techniques exist for extraction of these parameters from testing, such as those explored in Refs. [77]–[79]. However, given the substrate influence on the indentation modulus (Figure 13), several of these techniques are unsuitable for the present data. Nevertheless, using a phenomenological, power law description for the "steady state" yield strength [77], σ_s, we can extract activation parameters as follows:

$$\sigma_s = K\dot{\epsilon}^m \tag{2}$$

where K is a pre-exponential factor, $\dot{\epsilon}$ is the strain rate and m is the rate sensitivity. Next, we assume that the strain rate is governed by a thermally activated mechanism such that:

$$\dot{\epsilon} = B\exp\frac{-\Delta G^*}{kT} \tag{3}$$

$$\sigma_s = K'\exp\frac{-m\Delta G^*}{kT} \tag{4}$$

where B, K' are constants, k is the Boltzmann constant, and ΔG^* is the apparent activation enthalpy. From this description, we can calculate the apparent activation energy by obtaining the slope of $ln(\sigma_s)$ vs $\frac{m}{T}$, which suggests a Gibbs activation enthalpy of 12.7 kJ mol^{-1} or 0.13 eV for the AIF regime and 120 kJ mol^{-1} or 1.24 eV for the intermetallic regime. Strain rate sensitivity values were measured during indentation jump tests performed at each testing temperature. The activation volumes measured during jump tests at room temperature prior to microstructural coarsening are unusually high and were not used for activation parameter analysis; rather, activation volumes of 8 b^3, consistent with AIF-containing elevated temperature measurements as well as those reported in Ref. [28], were utilized for the room temperature activation volume when performing activation parameter analysis. All data measured (and utilized in these calculations) are presented in Table 1.

Focusing on the AIF regime, we can estimate the Helmholtz activation energy as described in Ref. [80] through the addition of the mechanical work as follows:

$$\Delta F = \Delta G^{*} + \Delta W$$
$$\Delta W = \nu_{act}\sigma = \nu_{act}\frac{H}{3} \qquad (5)$$

where ν_{act} is the activation volume, σ is the stress, and H is the hardness. This calculation results in a Helmholtz energy between 0.9 and 1.35 eV, which agrees excellently with that for STZ activity in a monolithic Al-based glass [81] or shear transformation zone (STZ) plasticity at grain boundaries [80]. While estimating STZ volume using such analysis is the subject of fervent debate, and may not provide physically meaningful information, using the formulation presented in Ref. [80], the STZ-size can be estimated by dividing the activation volume by the critical shear strain to initiate plasticity, assumed to be 0.2. This results in an estimated STZ volume for the Al-Ni-Ce alloy is between 0.7 and 1.1 nm^3, or 43-67 atoms, a similar size to the grain boundary spatial extent measured in Ref. [28].

These observations suggest that the rate limiting feature of the mechanical behavior of the AIF-containing Al-Ni-Ce alloy regime is STZ activity in the AIF-grain boundary regions, consistent with previous studies of crystalline-amorphous nanolaminates [82]. Other researchers have noted that such STZ-like grain boundary deformation displays a temperature dependence similar to that of the universal yield criterion for metallic glasses [76], [80]. Although this precise deformation mechanism has been argued to underpin the deleterious shear localization behavior in nanocrystalline metals at low temperatures [21], [80], STZ-like rate limiting deformation mechanisms provide intrinsic high temperature strength retention in our ternary alloy, suggesting that AIFs not only enhance microstructural stability and damage tolerance, but enable high temperature strength.

3.6 Predicting the transition in deformation behavior

The dramatic reduction in strength at 325 °C observed during elevated temperature indentation testing is due to intermetallic precipitation, eliminating the AIFs and enabling microstructural coarsening. This is evident not only in the reduction in room temperature strength collected after heating to 325 °C, but also in the activation analysis for these data. Activation parameter analysis suggests a Gibbs activation enthalpy of 1.24 eV for the precipitation regime, identical to dislocation-mediated behavior in UFG Al [79]. While this presents an apparent contradiction with the thermal stability observed during *in-* and *ex-situ* heating experiments (Figures 1 and 4), as the kinetics of intermetallic precipitation govern this transition, incorporating the testing time (2-3.5 hrs) into the interpretation of these data is essential. Thus, the mechanistic insight obtained through activation parameter analysis can be combined with the kinetic parameters obtained from our calorimetry (Figure 3) to predict the transition between the AIF-controlled and precipitation regimes, which is essential in designing materials for critical applications. Given the origin of this transition, we can apply the Kissinger analysis (Figure 3b) to estimate the transition temperature of mechanical properties due to precipitation. Since this method provides a relationship for peak temperature during non-isothermal conditions, it serves as a conservative estimate of this transition by calculating the peak temperatures for precipitation with an equivalent heating rate of the total thermal exposure per 1 °C. For instance, for a 30 min exposure, the equivalent heating rate would be $\frac{1^{\circ}C}{30min} \approx 5.54 \times 10^{-4}\frac{^{\circ}C}{s}$, corresponding to an estimated peak or transition temperature of 288 °C, in excellent agreement with the experimental data obtained during elevated temperature indentation testing. This transition temperature, as well as estimated transition temperatures for 2 and 1000 h at temperature, and corresponding activation parameter fits are included in Figure 12. These thermal estimates are quite conservative - Figure 1**c** demonstrates microstructural stability for 1 h at 325 °C, while the calorimetric model predicts stability for less than 10 min - but are useful for applications where retention of strength at temperature is critical. Such a simplistic model may also enable high-throughput screening of future novel alloys with the primary objective of increasing the precipitation peak temperature, enabling nanocrystalline alloy development for even higher temperature applications.

4. Conclusions

In conclusion, we have elucidated the structural origin of remarkable thermal stability and elevated temperature strength of an AIF-containing, nanocrystalline Al-Ni-Ce alloy. The results of our detailed *in-* and *ex-situ* thermal analysis, electron and X-ray diffraction, and elevated temperature indentation investigations allow us to draw the following conclusions:

- The presence and chemo-structural evolution of the AIFs present in the Al-Ni-Ce alloy gives rise to the exceptional microstructural stability of the alloy. Specifically, the reduction in the short-range order of the AIF during low temperature annealing due to solute enrichment reduces the propensity for intermetallic precipitation and stabilizes the nanocrystalline microstructure against grain growth up to high temperatures.

- High temperature indentation measurements show that the designed Al-Ni-Ce alloy exhibits strength retention that outperforms all high performance Al-alloys to date below 300 °C, and absolute strengths comparable with high performance alloys at higher temperatures, despite precipitation of intermetallic phases and coarsening of the microstructure.

- Analysis of the high temperature data suggest that grain boundary mediated STZ-like activity dominates the mechanical behavior prior to intermetallic precipitation, manifest in a weaker temperature dependence on strength than conventional Al-alloys.

- Finally, calorimetric analysis provides a conservative estimation of the transition temperature between AIF-controlled and precipitation-controlled mechanical properties.

These results not only demonstrate the scientific origin of the exceptional properties of this Al-Ni-Ce alloy, but also provide insight into alloy design strategies that embrace the presence of atomic disorder, ultimately leading to the creation of bulk [60] nanocrystalline alloys with exceptional high temperature performance.

Acknowledgements

This material is based upon work supported by the U.S. Department of Energy's Office of Energy Efficiency and Renewable Energy (EERE) under the Advanced Manufacturing Office Award Number DE-EE0009114. GHB acknowledges support from the National Science Foundation Graduate Research Fellowship under Grant No. 1650114. DK gratefully acknowledges funding from the European Research Council under grant agreement No. 771146 (TOUGHIT). DJS and JRT acknowledge support by the U.S. Department of Energy, Office of Science, Basic Energy Sciences, under Award No. DE-SC0021060. TJR acknowledges support by the U.S. Department of Energy, Office of Science, Basic Energy Sciences, under Award No. DE-SC0021224. This research used beamline 28-ID-1 of the National Synchrotron Light Source II, a U.S. Department of Energy (DOE) Office of Science User Facility operated for the DOE Office of Science by Brookhaven National Laboratory under Contract No. DE-SC0012704. The MRL Shared Experimental Facilities are supported by the MRSEC Program of the NSF under Award No. DMR 1720256; a member of the NSF-funded Materials Research Facilities Network (www.mrfn.org).

5. References

[**1**] V. Y. Gertsman and R. Birringer, “On the room-temperature grain growth in nanocrystalline copper,” *Scr. Metall. Mater.*, 1994, doi: 10.1016/0956-716X(94)90432-4.

[**2**] S. Singh *et al.*, “Ultrastable glasses from in silico vapour deposition,” *Nat. Mater.*, 2013, doi: 10.1038/nmat3521.

[**3**] J. Q. Wang *et al.*, “Increasing the kinetic stability of bulk metallic glasses,” *Acta Mater.*, 2016, doi: 10.1016/J.ACTAMAT.2015.11.048.

[**4**] T. Chookajorn *et al.*, “Design of Stable Nanocrystalline Alloys,” *Science (80-.).*, 2012, doi: 10.1126/science.1224737.

[**5**] H. Bin Yu *et al.*, “Ultrastable metallic glass,” *Adv. Mater.*, 2013, doi: 10.1002/adma.201302700.

[**6**] H. A. Murdoch and C. A. Schuh, “Estimation of grain boundary segregation enthalpy and its role in stable nanocrystalline alloy design,” *J. Mater. Res.*, 2019, doi: 10.1557/jmr.2013.211.

[**7**] J. Weissmüller, “Alloy effects in nanostructures,” *Nanostructured Mater.*, 1993, doi: 10.1016/0965-9773(93)90088-S.

[**8**] C. C. Koch *et al.*, “Stabilization of nanocrystalline grain sizes by solute additions,” *J. Mater. Sci.*, 2008, doi: 10.1007/s10853-008-2870-0.

[**9**] K. A. Darling *et al.*, “Grain size stabilization of nanocrystalline copper at high temperatures by alloying with tantalum,” *J. Alloys Compd.*, 2013, doi: 10.1016/j.jallcom.2013.03.177.

[**10**] K. A. Darling *et al.*, “Extreme creep resistance in a microstructurally stable nanocrystalline alloy,” *Nature*, 2016, doi: 10.1038/nature19313.

[**11**] O. K. Donaldson *et al.*, “Impurity stabilization of nanocrystalline grains in pulsed laser deposited tantalum,” *J. Mater. Res.*, 2017, doi: 10.1557/jmr.2017.68.

[**12**] L. Lu *et al.*, “Grain growth and strain release in nanocrystalline copper,” *J. Appl. Phys.*, 2001, doi: 10.1063/1.1367401.

[**13**] H. Natter *et al.*, “Nanocrystalline nickel and nickel-copper alloys: Synthesis, characterization, and thermal stability,” *J. Mater. Res.*, 1998, doi: 10.1557/JMR.1998.0169.

[**14**] K. A. Darling *et al.*, “Mitigating grain growth in binary nanocrystalline alloys through solute selection based on thermodynamic stability maps,” *Comput. Mater. Sci.*, 2014, doi: 10.1016/j.commatsci.2013.10.018.

[**15**] A. J. Detor and C. A. Schuh, “Microstructural evolution during the heat treatment of nanocrystalline alloys,” *J. Mater. Res.*, 2007, doi: 10.1557/jmr.2007.0403.

[**16**] O. K. Donaldson *et al.*, “Solute stabilization of nanocrystalline tungsten against abnormal

grain growth," *J. Mater. Res*, 2020, doi: 10.1557/jmr.2017.296.

[**17**] T. Y. Huang *et al.*, "Grain growth and second-phase precipitation in nanocrystalline aluminum-manganese electrodeposits," *J. Mater. Sci.*, doi: 10.1007/s10853-017-1764-4.

[**18**] A. Khalajhedayati and T. J. Rupert, "High-Temperature Stability and Grain Boundary Complexion Formation in a Nanocrystalline Cu-Zr Alloy," *JOM*, 2015, doi: 10.1007/s11837-015-1644-9.

[**19**] W. S. Cunningham *et al.*, "Suppressing irradiation induced grain growth and defect accumulation in nanocrystalline tungsten through grain boundary doping," *Acta Mater.*, 2021, doi: 10.1016/j.actamat.2021.116629.

[**20**] A. Khalajhedayati and T. J. Rupert, "No Title," *Sci. Rep.*, 2015, doi: 10.1038/srep10663.

[**21**] J. Lohmiller *et al.*, "The effect of solute segregation on strain localization in nanocrystalline thin films: Dislocation glide vs. grain-boundary mediated plasticity," *Appl. Phys. Lett.*, 2013, doi: 10.1063/1.4811743.

[**22**] J. G. Kaufman, *Fire Resistance of Aluminum and Aluminum Alloys*. 2016.

[**23**] Z. C. Sims *et al.*, "High performance aluminum–cerium alloys for high-temperature applications," *Mater. Horizons*, 2017, doi: 10.1039/C7MH00391A.

[**24**] A. B. Pandey, **"**High temperature aluminum alloys,**"** US 7,875,132 B2**,** May-2011.

[**25**] Z. C. Sims *et al.*, "Cerium-Based, Intermetallic-Strengthened Aluminum Casting Alloy: High-Volume Co-product Development," *JOM*, 2016, doi: 10.1007/s11837-016-1943-9.

[**26**] A. Devaraj *et al.*, "Grain boundary segregation and intermetallic precipitation in coarsening resistant nanocrystalline aluminum alloys," *Acta Mater.*, 2019, doi: 10.1016/j.actamat.2018.09.038.

[**27**] J. A. Carpenter *et al.*, "Road transportation vehicles," *MRS Bull.*, 2008, doi: 10.1557/mrs2008.86.

[**28**] G. H. Balbus *et al.*, "Suppression of shear localization in nanocrystalline Al–Ni–Ce via segregation engineering," *Acta Mater.*, 2020, doi: 10.1016/j.actamat.2020.01.041.

[**29**] J. D. Schuler and T. J. Rupert, "Materials selection rules for amorphous complexion formation in binary metallic alloys," *Acta Mater.*, 2017.

[**30**] C. M. Grigorian and T. J. Rupert, "Thick amorphous complexion formation and extreme thermal stability in ternary nanocrystalline Cu-Zr-Hf alloys," *Acta Mater.*, 2019.

[**31**] A. Khalajhedayati *et al.*, "Manipulating the interfacial structure of nanomaterials to achieve a unique combination of strength and ductility," *Nat. Commun.*, 2016, doi: 10.1038/ncomms10802.

[**32**] J. D. Schuler *et al.*, "Amorphous intergranular films mitigate radiation damage in nanocrystalline Cu-Zr," *Acta Mater.*, 2020, doi: 10.1016/j.actamat.2019.12.048.

[**33**] F. de la Pena *et al.*, “Electron Microscopy (Big and Small) Data Analysis With the Open Source Software Package HyperSpy,” *Microsc. Microanal.*, 2017, doi: 10.1017/s1431927617001751.

[**34**] “EMsoft-org/EMsoft: Release 4.2 to synchronize with DI tutorial paper | Zenodo.” [Online]. Available: https://zenodo.org/record/2581285#.X34XzWhKhPY. [Accessed: 07-Oct-2020].

[**35**] A. Jain *et al.*, “Commentary: The materials project: A materials genome approach to accelerating materials innovation,” *APL Materials*, vol. 1, no. 1. American Institute of Physics Inc., p. 011002, 18-Jul-2013, doi: 10.1063/1.4812323.

[**36**] T. Chookajorn and C. A. Schuh, “Thermodynamics of stable nanocrystalline alloys: A Monte Carlo analysis,” *Phys. Rev. B*, 2014, doi: 10.1103/PhysRevB.89.064102.

[**37**] A. R. Kalidindi *et al.*, “Nanocrystalline Materials at Equilibrium: A Thermodynamic Review,” *JOM*, vol. 67, no. 12. Minerals, Metals and Materials Society, pp. 2834–2843, 01-Dec-2015, doi: 10.1007/s11837-015-1636-9.

[**38**] A. R. Kalidindi and C. A. Schuh, “A compound unit method for incorporating ordered compounds into lattice models of alloys,” *Comput. Mater. Sci.*, 2016, doi: 10.1016/j.commatsci.2016.02.039.

[**39**] W. Xing *et al.*, “Preferred nanocrystalline configurations in ternary and multicomponent alloys,” *Scr. Mater.*, 2017, doi: 10.1016/j.scriptamat.2016.09.014.

[**40**] W. Xing *et al.*, “Solute interaction effects on grain boundary segregation in ternary alloys,” *Acta Mater.*, 2018, doi: 10.1016/j.actamat.2018.09.005.

[**41**] K. M. Ø. Jensen *et al.*, “Demonstration of thin film pair distribution function analysis (tfPDF) for the study of local structure in amorphous and crystalline thin films,” in *IUCrJ*, 2015, vol. 2, no. 5, pp. 481–489, doi: 10.1107/S2052252515012221.

[**42**] X. Shi *et al.*, “Performance calculations of the X-ray powder diffraction beamline at NSLS-II,” *J. Synchrotron Radiat.*, 2013, doi: 10.1107/S0909049512049175.

[**43**] W. C. Oliver and G. M. Pharr, “An improved technique for determining hardness and elastic modulus using load and displacement sensing indentation experiments,” *J. Mater. Res.*, 1992, doi: 10.1557/JMR.1992.1564.

[**44**] A. Inoue, “Stabilization of metallic supercooled liquid and bulk amorphous alloys,” *Acta Mater.*, 2000, doi: 10.1016/S1359-6454(99)00300-6.

[**45**] K. Hono *et al.*, “Solute partitioning in partially crystallized Al-Ni-Ce(-Cu) metallic glasses,” *Scr. Metall. Mater.*, 1995, doi: 10.1016/S0956-716X(99)80035-1.

[**46**] X. Zhou *et al.*, “Grain Boundary Specific Segregation in Nanocrystalline Fe(Cr),” *Sci. Rep.*, 2016, doi: 10.1038/srep34642.

[**47**] M. Mantina *et al.*, “3d transition metal impurities in aluminum: A first-principles study,” *Phys. Rev. B*, 2009, doi: 10.1103/PhysRevB.80.184111.

[**48**] D. Simonovic and M. H. F. F. Sluiter, "Impurity diffusion activation energies in Al from first principles," *Phys. Rev. B*, 2009, doi: 10.1103/PhysRevB.79.054304.

[**49**] K. Song *et al.*, "Compositional dependence of glass-forming ability, medium-range order, thermal stability and liquid fragility of Al-Ni-Ce-based amorphous alloys," *Mater. Sci. Eng. A*, 2009, doi: 10.1016/j.msea.2008.11.043.

[**50**] A. P. Tsai *et al.*, "Formation and precipitation mechanism of nanoscale Al particles in Al-Ni base amorphous alloys," *Acta Mater.*, 1997, doi: 10.1016/S1359-6454(96)00268-6.

[**51**] X. P. P. Li *et al.*, "Crystallization behaviour and thermal stability of two aluminium-based metallic glass powder materials," *Mater. Sci. Eng. A*, 2011, doi: 10.1016/j.msea.2011.09.107.

[**52**] H. Yang *et al.*, "Glass formation and microstructure evolution in Al-Ni-RE (RE = La, Ce, Pr, Nd and misch metal) ternary systems," *Philos. Mag.*, 2007, doi: 10.1080/14786430701537961.

[**53**] H. Wang *et al.*, "Thermodynamic Optimization of the Ni-Al-Ce Ternary System," *J. Phase Equilibria Diffus.*, 2016, doi: 10.1007/s11669-015-0447-6.

[**54**] A. Hawksworth *et al.*, "Thermal stability of Al/Al11Ce3 and Al/Al11La3/Al3Ni eutectics obtained by Bridgman growth," *Mater. Sci. Technol.*, 1999, doi: 10.1179/026708399101506346.

[**55**] S. Sohn *et al.*, "Nanoscale size effects in crystallization of metallic glass nanorods," *Nat. Commun.*, 2015, doi: 10.1038/ncomms9157.

[**56**] V. Turlo and T. J. Rupert, "Linear Complexions: Metastable Phase Formation and Coexistence at Dislocations," *Phys. Rev. Lett.*, 2019, doi: 10.1103/PhysRevLett.122.126102.

[**57**] C. Kittel and D. F. Holcomb, "Introduction to Solid State Physics," *Am. J. Phys.*, 1967, doi: 10.1119/1.1974177.

[**58**] A. Takeuchi and A. Inoue, "Calculations of Mixing Enthalpy and Mismatch Entropy for Ternary Amorphous Alloys," *Mater. Trans. JIM*, 2000, doi: 10.2320/matertrans1989.41.1372.

[**59**] M. A. Atwater and K. A. Darling, *A Visual Library of Stability in Binary Metallic Systems: The Stabilization of Nanocrystalline Grain Size by Solute Addition: Part 1*. 2012.

[**60**] O. K. Donaldson and T. J. Rupert, "Amorphous Intergranular Films Enable the Creation of Bulk Nanocrystalline Cu-Zr with Full Density," 2019.

[**61**] A. R. Kalidindi and C. A. Schuh, "Stability criteria for nanocrystalline alloys," *Acta Mater.*, 2017, doi: 10.1016/j.actamat.2017.03.029.

[**62**] P. Juhás *et al.*, "PDFgetX3: A rapid and highly automatable program for processing powder diffraction data into total scattering pair distribution functions," *J. Appl. Crystallogr.*, 2013, doi: 10.1107/S0021889813005190.

[**63**] M. Wilson and P. A. Madden, “Prepeaks and first sharp diffraction peaks in computer simulations of strong and fragile ionic liquids,” *Phys. Rev. Lett.*, 1994, doi: 10.1103/PhysRevLett.72.3033.

[**64**] H. Y. Hsieh *et al.*, “Short range ordering in amorphous Al90FexCe10-x,” *J. Non. Cryst. Solids*, 1991, doi: 10.1016/0022-3093(91)90427-8.

[**65**] M. Maret *et al.*, “Structure of liquid Al80Ni20 alloy,” *Phys. Rev. B*, 1990, doi: 10.1103/PhysRevB.42.1598.

[**66**] F. Zhang *et al.*, “Solute–solute correlations responsible for the prepeak in structure factors of undercooled Al-rich liquids: a molecular dynamics study,” *J. Phys. Condens. Matter*, 2015, doi: 10.1088/0953-8984/27/20/205701.

[**67**] L. Hu *et al.*, “Liquid fragility and characteristic of the structure corresponding to the prepeak of AlNiCe amorphous alloys,” *Acta Mater.*, 2004, doi: 10.1016/j.actamat.2004.06.035.

[**68**] Y. E. Kalay *et al.*, “Local structure in marginal glass forming Al-Sm alloy,” *Intermetallics*, 2010, doi: 10.1016/j.intermet.2010.05.005.

[**69**] L. Wang *et al.*, “Grain rotation mediated by grain boundary dislocations in nanocrystalline platinum,” *Nat. Commun.*, 2014, doi: 10.1038/ncomms5402.

[**70**] Z. C. Cordero *et al.*, “Six decades of the Hall–Petch effect – a survey of grain-size strengthening studies on pure metals,” *Int. Mater. Rev.*, 2016, doi: 10.1080/09506608.2016.1191808.

[**71**] D. J. Magagnosc *et al.*, “Isochemical control over structural state and mechanical properties in Pd-based metallic glass by sputter deposition at elevated temperatures,” *APL Mater.*, 2016, doi: 10.1063/1.4960388.

[**72**] D. Tabor, *The hardness of metals*. Clarendon Press, 2000.

[**73**] J. L. Hay *et al.*, “Using the Ratio of Loading Slope and Elastic Stiffness to Predict Pile-Up and Constraint Factor During Indentation,” *MRS Proc.*, 1998, doi: 10.1557/PROC-522-101.

[**74**] A. C. Lund *et al.*, “Tension/compression strength asymmetry in a simulated nanocrystalline metal,” *Phys. Rev. B*, 2004, doi: 10.1103/PhysRevB.69.012101.

[**75**] Q. Li *et al.*, “High temperature thermal and mechanical stability of high-strength nanotwinned Al alloys,” *Acta Mater.*, 2019, doi: 10.1016/j.actamat.2018.11.011.

[**76**] W. L. Johnson and K. Samwer, “A Universal Criterion for Plastic Yielding of Metallic Glasses with a (T/Tg)^(2/3) Temperature Dependence,” *Phys. Rev. Lett.*, 2005, doi: 10.1103/PhysRevLett.95.195501.

[**77**] G. Mohanty *et al.*, “Elevated temperature, strain rate jump microcompression of nanocrystalline nickel,” *Philos. Mag.*, 2015, doi: 10.1080/14786435.2014.951709.

[**78**] O. D. Sherby and P. E. Armstrong, “Prediction of Activation Energies for Creep and Self-

Diffusion from Hot Hardness Data."

[**79**] J. M. Wheeler *et al.*, "Activation parameters for deformation of ultrafine-grained aluminium as determined by indentation strain rate jumps at elevated temperature," *Mater. Sci. Eng. A*, 2013, doi: 10.1016/j.msea.2013.07.033.

[**80**] M. Grewer and R. Birringer, "Shear shuffling governs plastic flow in nanocrystalline metals: An analysis of thermal activation parameters," *Phys. Rev. B*, 2014, doi: 10.1103/PhysRevB.89.184108.

[**81**] J. D. Ju *et al.*, "An atomically quantized hierarchy of shear transformation zones in a metallic glass," *J. Appl. Phys.*, 2011, doi: 10.1063/1.3552300.

[**82**] B. Cheng and J. R. Trelewicz, "Design of crystalline-amorphous nanolaminates using deformation mechanism maps," *Acta Mater.*, 2018, doi: 10.1016/j.actamat.2018.05.006.

[**83**] L. Ajdelsztajn *et al.*, "Cold Spray Deposition of Nanocrystalline Aluminum Alloys," *Metall. Mater. Trans. A*, 2005.

[**84**] A. R. Yavari *et al.*, "Nanostructured bulk Al90Fe5Nd5 prepared by cold consolidation of gas atomised powder using severe plastic deformation," *Scr. Mater.*, 2002, doi: 10.1016/S1359-6462(02)00057-X.

[**85**] H. J. Choi *et al.*, "Tensile behavior of bulk nanocrystalline aluminum synthesized by hot extrusion of ball-milled powders," *Scr. Mater.*, 2008, doi: 10.1016/j.scriptamat.2008.07.030.

[**86**] S. C. Pun *et al.*, "Nanocrystalline Al-Mg with extreme strength due to grain boundary doping," *Mater. Sci. Eng. A*, 2017.

[**87**] J. K. Rana *et al.*, "Microstructure and mechanical properties of nanocrystalline high strength Al–Mg–Si (AA6061) alloy by high energy ball milling and spark plasma sintering," *Mater. Sci. Eng. A*, 2009, doi: 10.1016/j.msea.2009.08.041.

[**88**] M. N. Rittner *et al.*, "Structure-property correlations in nanocrystalline Al-Zr alloy composites," *Acta Mater.*, 1996, doi: 10.1016/1359-6454(95)00303-7.

[**89**] M. N. Rittner *et al.*, "Mechanical behavior of nanocrystalline aluminum-zirconium," *Mater. Sci. Eng. A*, 1997, doi: 10.1016/S0921-5093(97)00129-9.

[**90**] S. Ruan and C. A. Schuh, "Electrodeposited Al–Mn alloys with microcrystalline, nanocrystalline, amorphous and nano-quasicrystalline structures," *Acta Mater.*, 2009, doi: 10.1016/J.ACTAMAT.2009.04.030.

[**91**] R. Z. Valiev *et al.*, "On the origin of the extremely high strength of ultrafine-grained Al alloys produced by severe plastic deformation," *Scr. Mater.*, 2010, doi: 10.1016/J.SCRIPTAMAT.2010.07.014.

[**92**] D. B. Witkin and E. J. Lavernia, "Synthesis and mechanical behavior of nanostructured materials via cryomilling," *Prog. Mater. Sci.*, 2006, doi: 10.1016/J.PMATSCI.2005.04.004.

[**93**] R. W. Armstrong *et al.*, “Elastic, plastic and cracking indentation behavior of silicon crystals,” *Mater. Sci. Eng. A*, 1996, doi: 10.1016/0921-5093(95)10148-9.

[**94**] V. Maier-Kiener and K. Durst, “Advanced Nanoindentation Testing for Studying Strain-Rate Sensitivity and Activation Volume,” *JOM*, 2017, doi: 10.1007/s11837-017-2536-y.

[**95**] V. Maier *et al.*, “Nanoindentation strain-rate jump tests for determining the local strain-rate sensitivity in nanocrystalline Ni and ultrafine-grained Al,” *J. Mater. Res.*, 2011, doi: 10.1557/jmr.2011.156.

Tables

Table 1: Summary of elevated temperature indentation testing – testing temperature, previous thermal exposure, hardness, and rate sensitivity measurements.

Test Temperature (˚C)	**Previous Exposure (˚C)**	**H_o (GPa)**	**Activation Volume (b^3)**	**Strain Rate Sensitivity, *m***
25	25	5.16 ± 0.04	123 ± 54*	0.0023 ± 0.0007
25	200	5.43 ± 0.07	181 ± 84*	0.0016 ± 0.0008
25	250	5.42 ± 0.06	207 ± 119*	0.0015 ± 0.0007
25	325	3.05 ± 0.11	11 ± 1	0.0373 ± 0.0026
100	25	4.81 ± 0.15	32 ± 21	0.0140 ± 0.0060
200	25	4.52 ± 0.07	10 ± 2	0.0501 ± 0.0091
250	25	4.04 ± 0.11	6 ± 1	0.1000 ± 0.0150
325	25	0.67 ± 0.07	31 ± 2	0.1390 ± 0.0076

* All activation parameter calculations were performed using a room temp (25 °C) activation volume of 8 b^3 from Ref. [28]. The origin of the large room temperature activation volume data measured in the Al-Ni-Ce alloy during jump testing is actively being investigated.

Figures

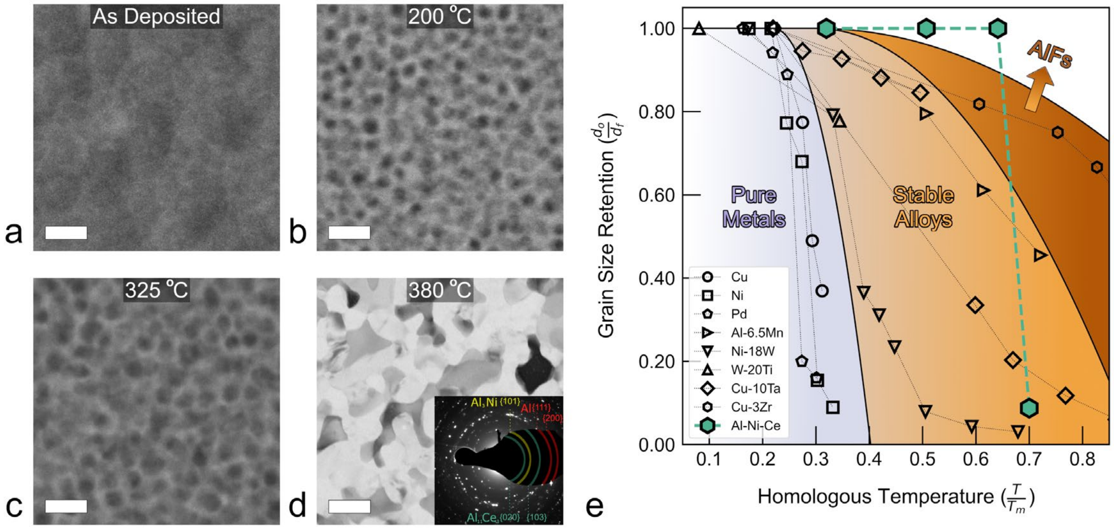

Figure 1: *Ex-situ thermal stability analysis.* ***a-d****, HAADF (****a-c****) and BF (****d****) micrographs of samples in the as-deposited condition (****a****), and annealed for one h at temperatures of 200 °C, 325 °C, and 380 °C. Scale bars are 10 nm in* ***a-c*** *and 100 nm in* ***d****.* ***b-c*** *exhibit chemical segregation of high mass elements (Ni, Ce) to grain boundaries (bright), resulting in Al rich grain interiors (dark);* ***d****, provides evidence of intermetallic precipitation and grain growth. Inset is a diffraction pattern shown the presence of* Al_3Ni *(yellow {101}),* $Al_{11}Ce_3$ *(green {020} and {103}) and Al (red, {111} and {200}).* ***e****, Grain size retention for several thermally stable nanocrystalline alloys, alongside the Al-Ni-Ce alloy, as a function of homologous temperature. Data from [9], [12], [13], [15]–[18].*

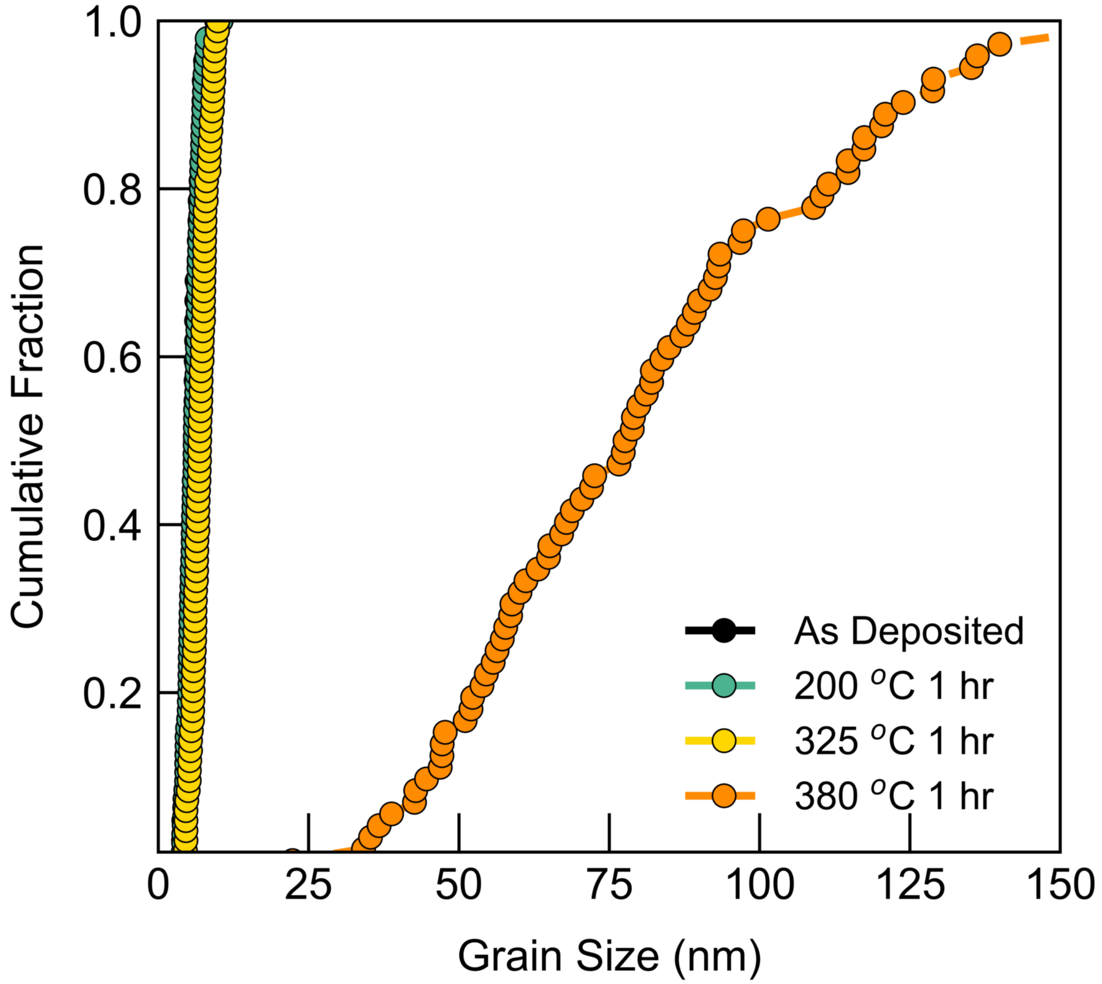

Figure 2: *Cumulative grain size distributions measured from dark field TEM experiments of ex-situ annealed Al-Ni-Ce alloy samples.*

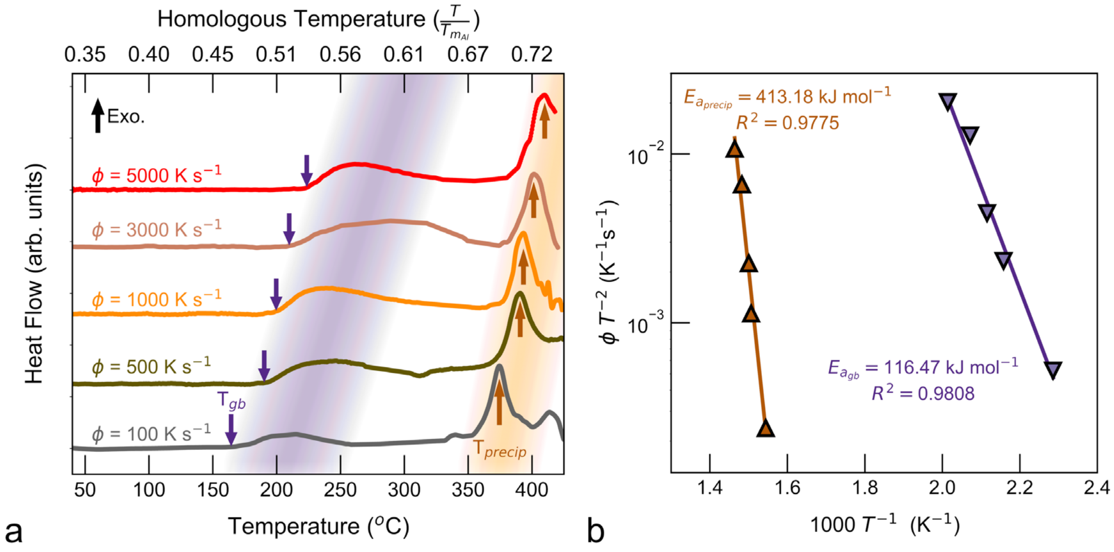

Figure 3: *Ex-situ differential scanning calorimetry.* ***a*** *DSC heat flows with arrows noting onset and peak temperatures of the low (T_{gb}) and high (T_{precip}) temperature exothermic events, respectively.* ***b****, Kissinger analysis of the two primary exothermic events noted in* ***a****.*

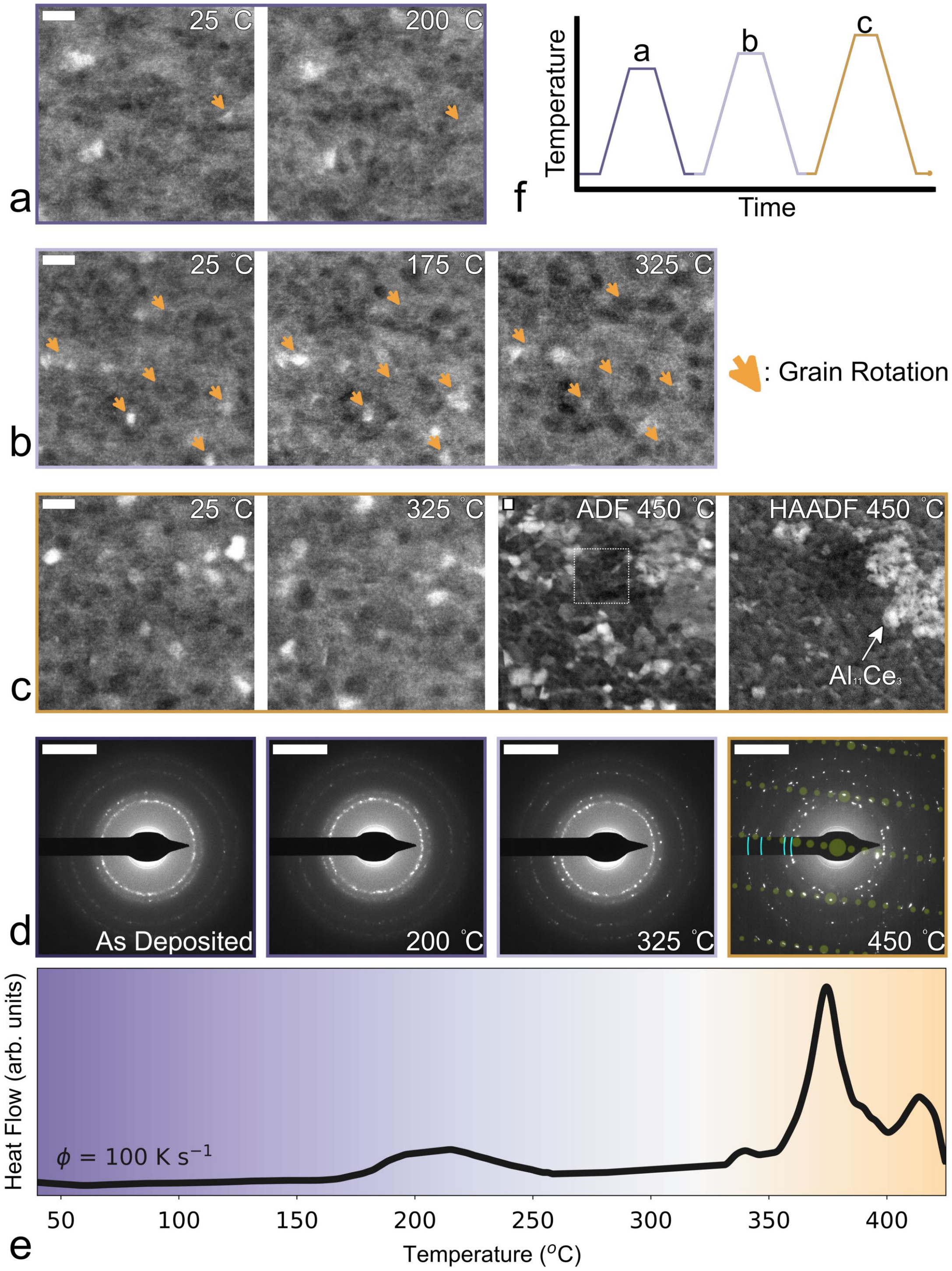

Figure 4: *In-situ TEM heating experiments.* ***a-c****, Annular dark field (ADF) STEM micrographs collected during separate heating segments up to 200 °C, 325 °C, and 450 °C. Instances of grain reorientation are noted by orange arrows. Scale bars are 10 nm.* ***c*** *also contains a HAADF STEM micrograph collected during final heating sequence up to 450 °C. Dashed region in 450 °C ADF micrograph is the original area imaged at 25 - 325 °C.* ***d****, Selected area diffraction patterns collected at room temperature after heating to temperature noted. Scale bars are 5*

nm^{-1}. Slight evolution in the diffraction patterns is evident at 325 °C, corresponding to reorientation events noted by arrows in ***b****. Simulated electron diffraction pattern of a [011] zone axis of α- Al$_{11}$Ce$_3$ is overlaid in green for comparison to 450 °C diffraction pattern collected from intermetallics in* ***c****. {111}, {200}, {220} and {311} Al diffraction rings are noted in blue along the beam-stop.* ***e****, DSC heat flow curve from ex-situ analysis for comparison of thermal signatures to direct observations.* ***f****, Schematic of experimental heating profile.*

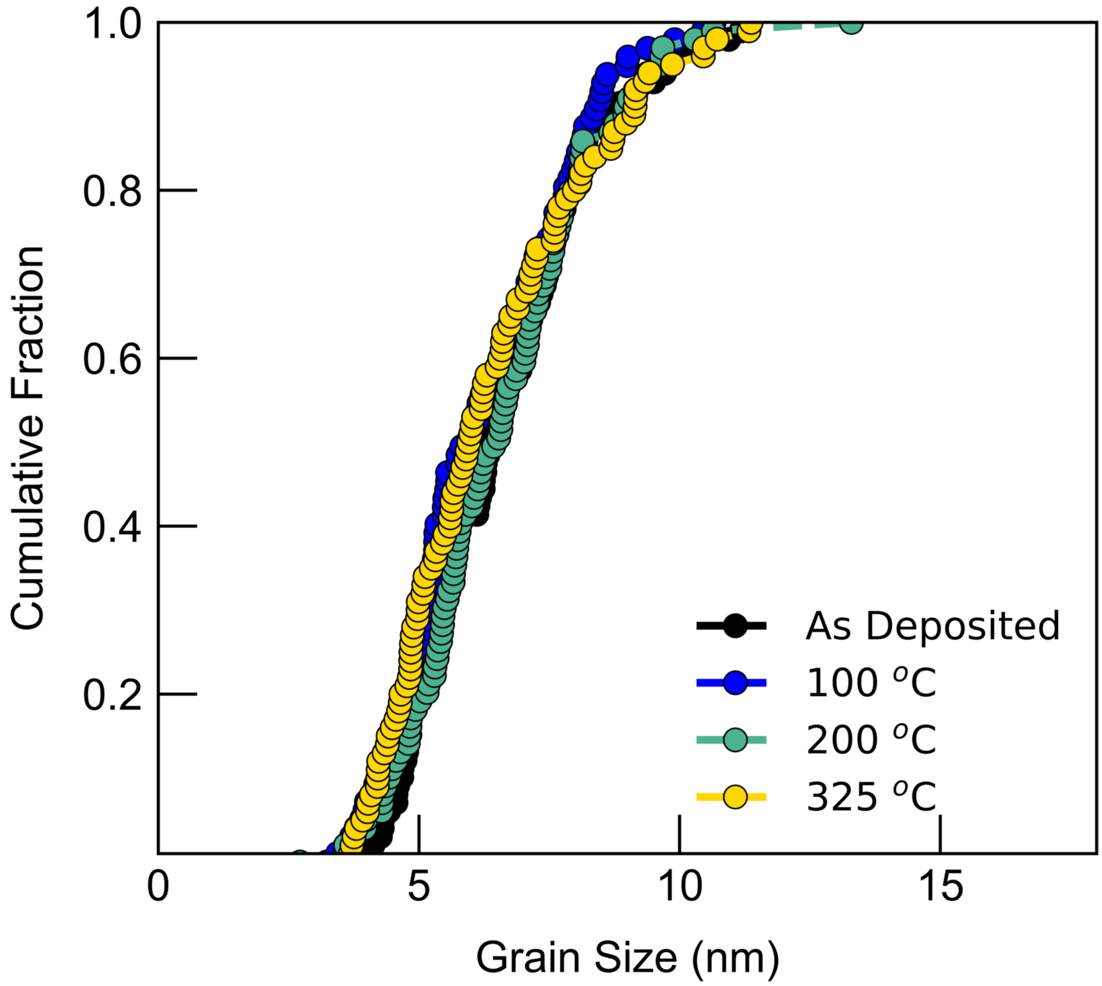

Figure 5: *Grain size cumulative area distributions derived from conventional dark field TEM images during in-situ heating experiments.*

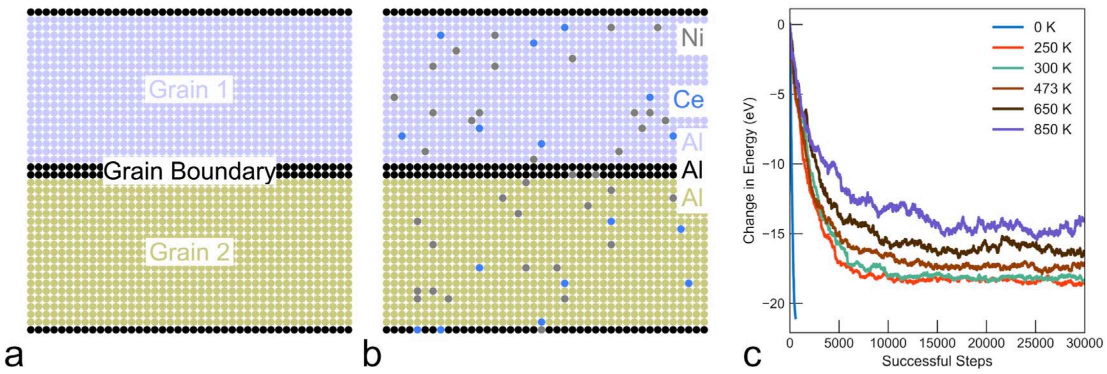

Figure 6: ***a***, *2D projection of bi-crystal Monte Carlo initialization demonstrating the grain boundary and grain interior sites.* ***b***, *2D projection of the random chemical initialization for the ternary* $Al_{97}Ni_2Ce_1$ *simulation. c, Net change in energy of simulation cell as a function of successful Monte Carlo steps in* $Al_{97}Ni_2Ce_1$*. The change in energy was calculated by subtracting the total system energy at each step by the initial system energy.*

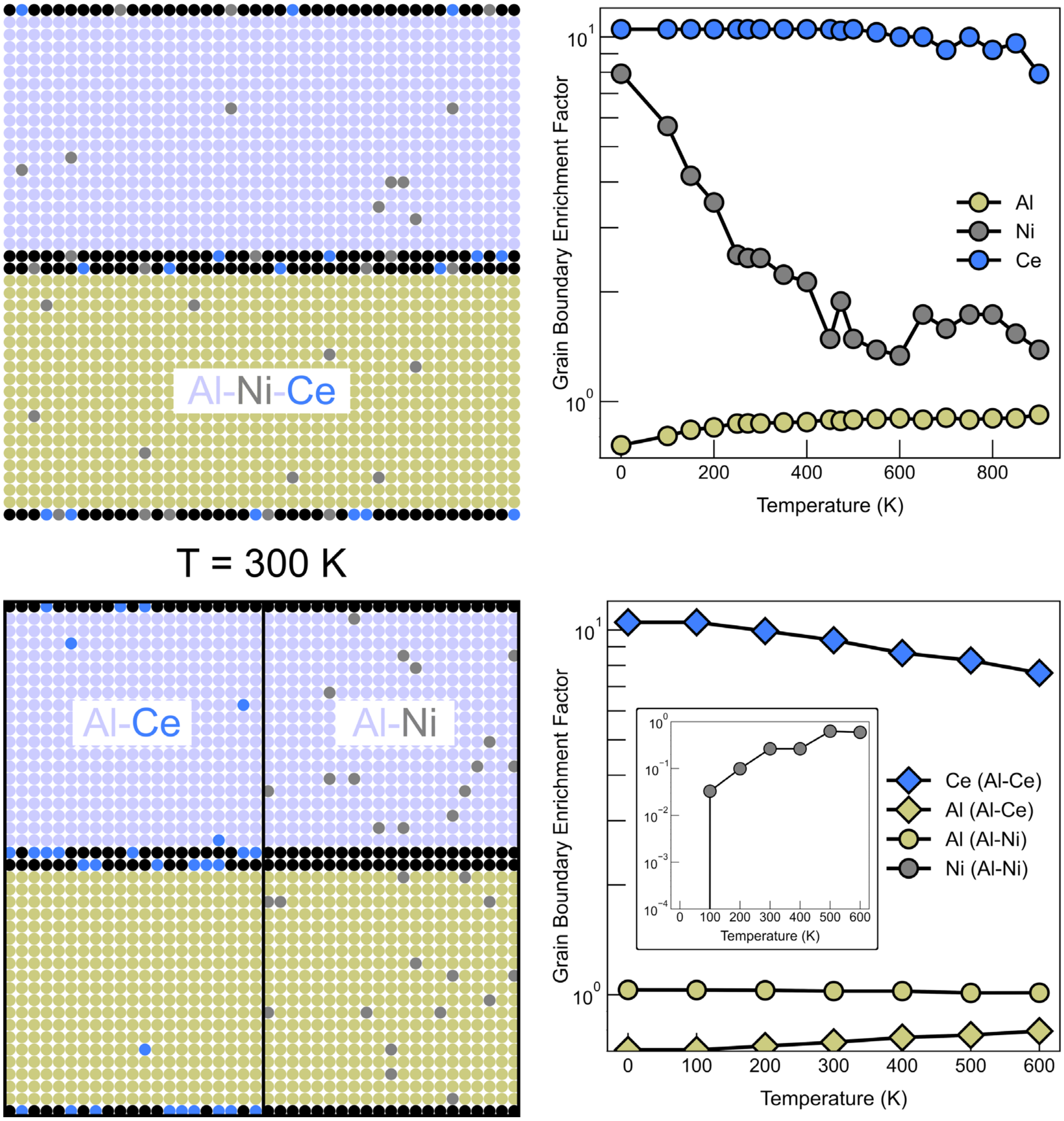

Figure 7: *Equilibrated 2D snapshots of ternary* $Al_{97}Ni_2Ce_1$ *(top left) and binary* $Al_{98}Ni_2$ *and* $Al_{98}Ce_2$ *(bottom left) at 300K. The ternary system shows enrichment of the grain boundary in both Ni and Ce, whereas only the binary Al-Ce exhibits grain boundary enrichment. This is quantitatively shown in the grain boundary enrichment figures on the right.*

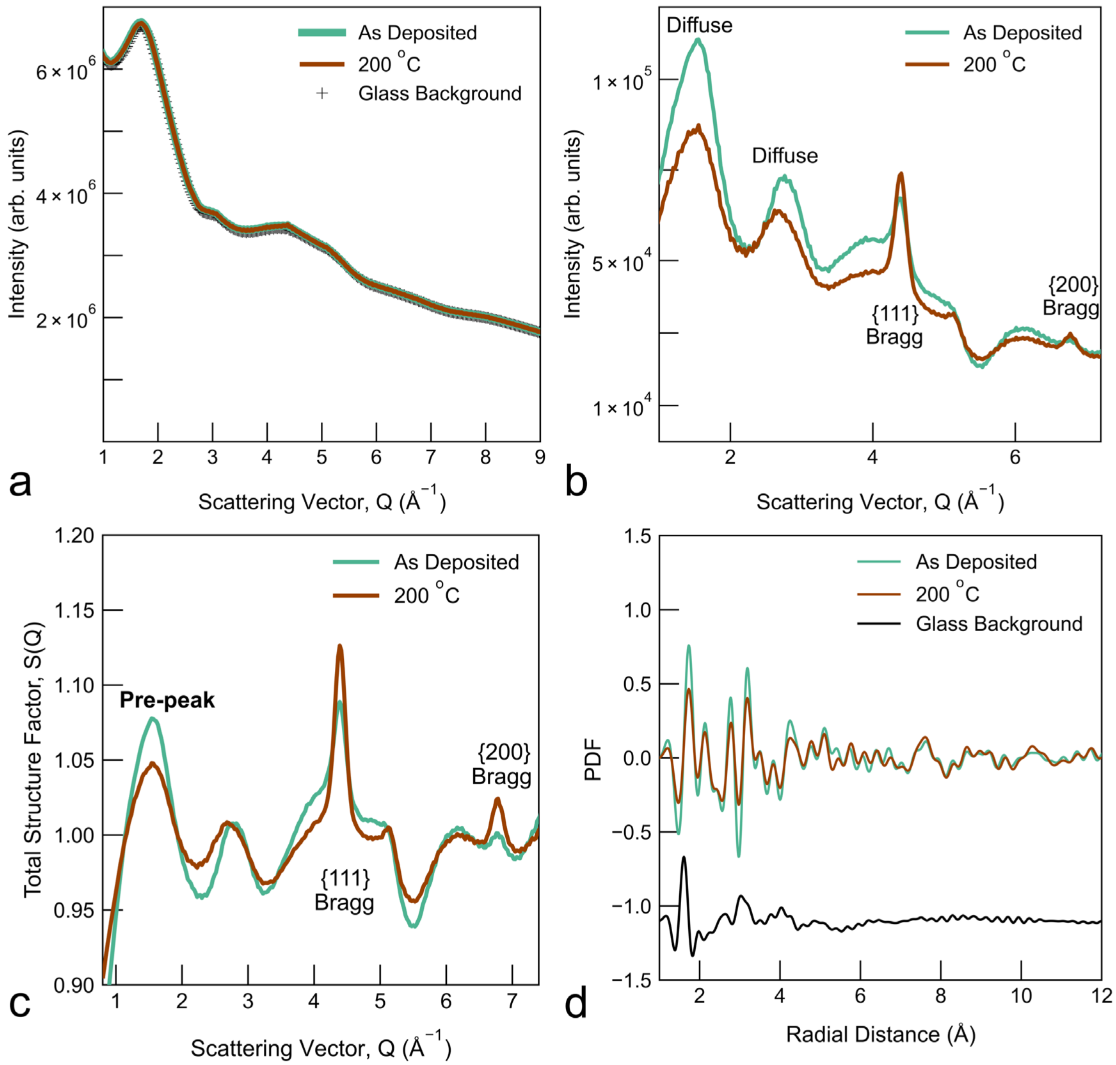

Figure 8: ***a***, *Radially integrated total scattering patterns for thin film X-ray experiments.* ***b***, *Background subtracted, radially integrated total scattering patterns for thin film X-ray experiments. Two types of features are noted: 'diffuse' features from the amorphous structure and 'Bragg' features from crystalline domains.* ***c***, *Total structure factors derived for the as deposited and annealed (200 °C, 1 h) sample. The large pre-peak at* ≈ 1.5 Å^{-1} *and Bragg peaks at {111} and {200} {hkl}s are noted.* ***d***, *Atomic PDFs showing short-range atomic correlations in as deposited and annealed specimens, as well as for the glass substrate.*

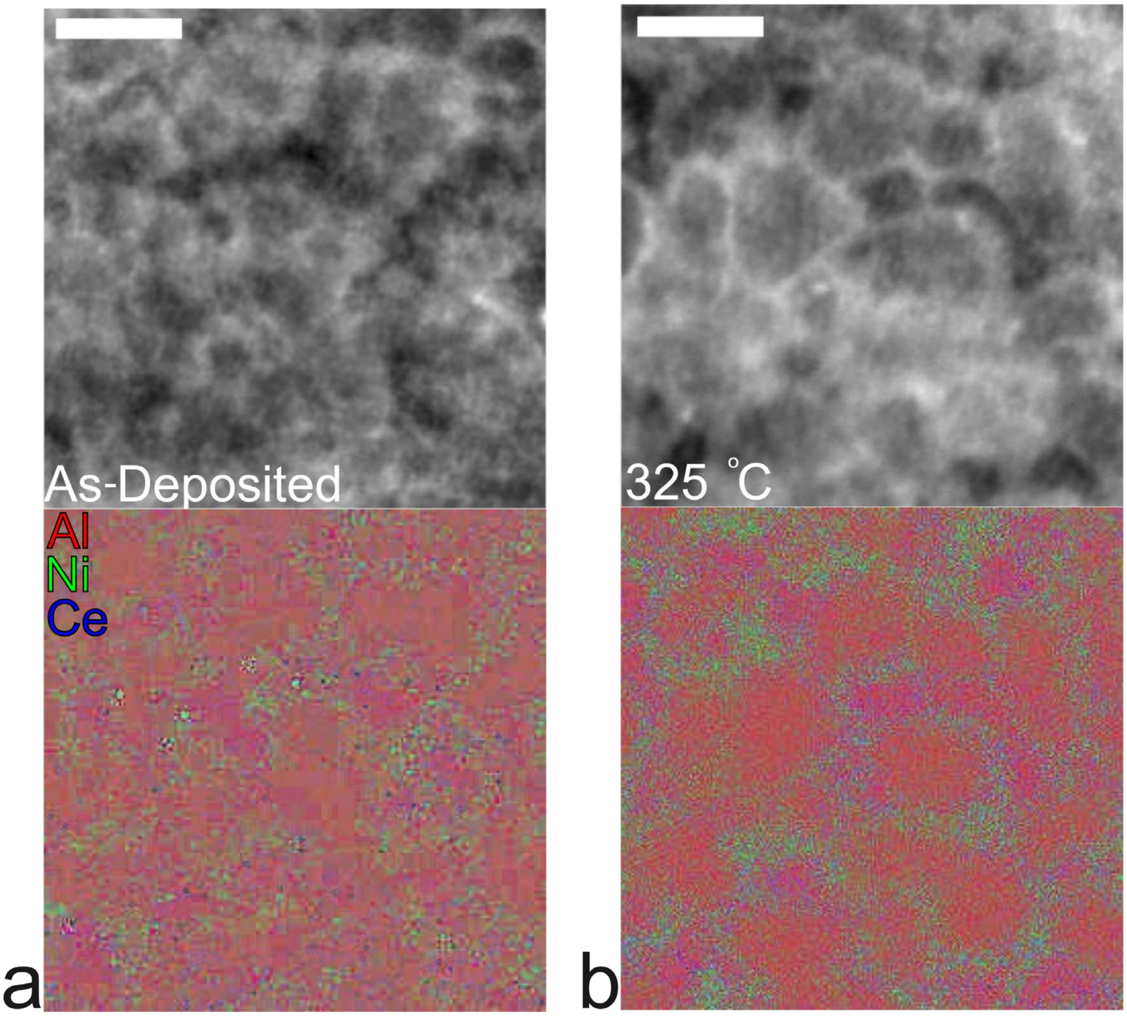

Figure 9: ***a***, ***b***, *HAADF-STEM and electron dispersive X-ray spectroscopy (EDS) maps of the as-deposited (****a****) and heated (****b****, 325 °C, in-situ) Al-Ni-Ce sample. Scale bars are 10 nm. The EDS maps are color coded: Al is red, Ce is blue, and Ni is yellow. The color intensity corresponds to the local concentration in atomic percent, scaled to the minimum and maximum values. The range of compositions reflected in the color intensities in* ***a*** *are [94, 95] % Al, [3.5, 4.1] % Ni and [1.32, 1.35] % Ce, and for* ***b*** *[94, 97] % Al, [0, 6.3] % Ni and [0, 3.4] % Ce, respectively.*

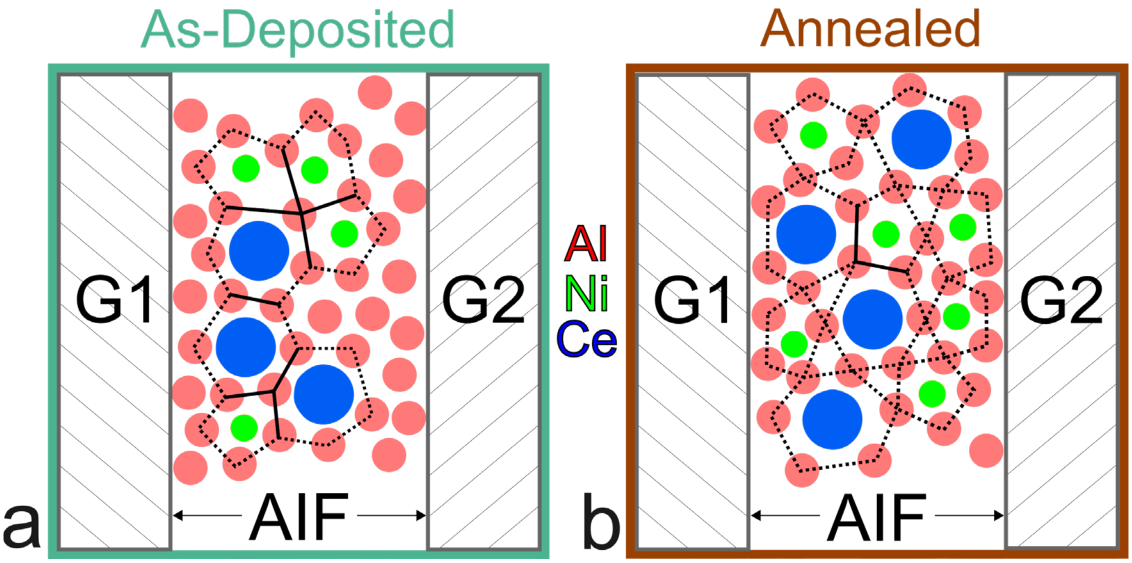

***Figure 10: a**, **b**, Schematic evolution of hypothesized solute-centered polyhedral packing within the AIF between two neighboring grains (G1 and G2, hatched) in the as-deposited and annealed states. Dashed lines indicate solute-centered polyhedra, which exhibit more vertex sharing with annealing. Edge sharing faces are noted by solid lines.*

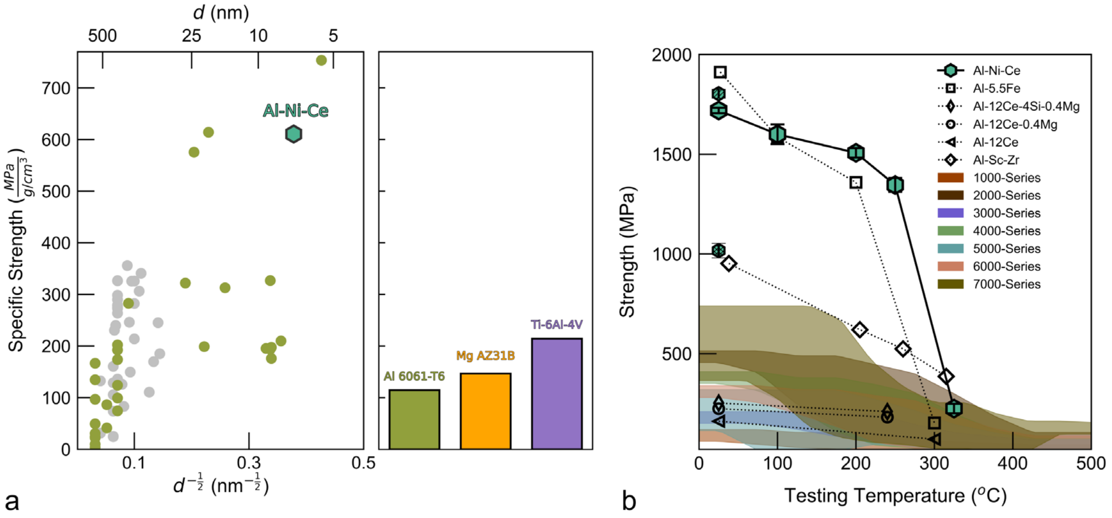

***Figure 11: a**, Left, estimated specific strength of Al alloys as a function of grain size. Data measured by indentation is colored in green. Right, high specific strength alloys Ti-6Al-4V, Mg AZ31B, and Al 6061-T6 included for reference. Data from references* [75], [83]–[92]. ***b**, Elevated temperature mechanical properties of the Al-Ni-Ce alloy, alongside conventional (1XXX-7XXX series) alloys, Sc and Ce containing alloys, and other high performance Al-alloys (data from* [22]–[25], [75]*). Error bars for the Al-Ni-Ce sample are within the marker. The maximum room temperature strength was recorded after heating to 250 °C is noted by the single hatched hexagonal marker. The room temperature strength after heating to 325 °C is noted by the cross hatched hexagonal marker.*

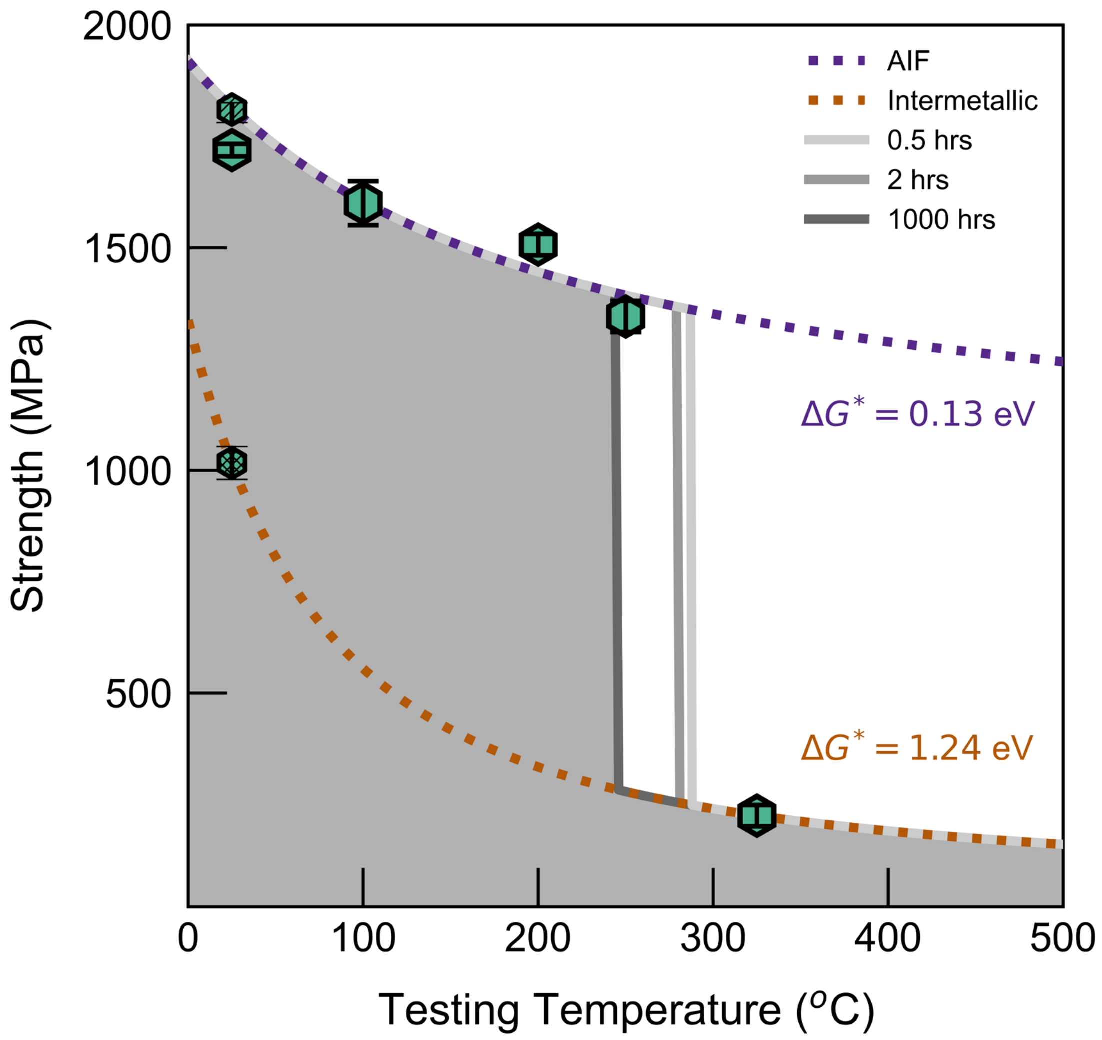

Figure 12: *Projected transition temperatures for various time exposures from calorimetric modeling, alongside strength and activation parameter analysis above.*

Appendix A: Substrate influence during indentation

Room temperature hardness and modulus data for thirteen indents performed on the as-deposited material are presented in Figure A.1, demonstrating the influence of the Si substrate. The modulus data is significantly affected by the substrate, whereas the hardness data is largely substrate insensitive. This can be ascertained as the hardness of single crystal (100) Si exceeds 10 GPa [93], but a significant increase in hardness at large depths is absent in Figure A.1. Thus, while the hardness data presented is extracted from depths larger than 10% of the film thickness (100 nm), the hardness values are representative of intrinsic material behavior. The depth selected for hardness measurements was chosen to optimize between minimal substrate influence and was enough penetration to minimize geometrical inaccuracies, instabilities, and transient behavior of the testing platform. Furthermore, the hardness values are not significantly different than those extracted from an indentation depth of 100, but the stability of the testing platform improves at larger penetration depths at elevated temperature. Strain rate jump tests were performed at all testing temperatures by reducing the strain rate from 0.1 s^{-1} to 0.01 s^{-1} at a depth of 200 nm, and jumping back to 0.1 s^{-1} at a depth of 350 nm to elucidate the strain rate sensitivities and activation volumes, as described in Refs. [94], [95].

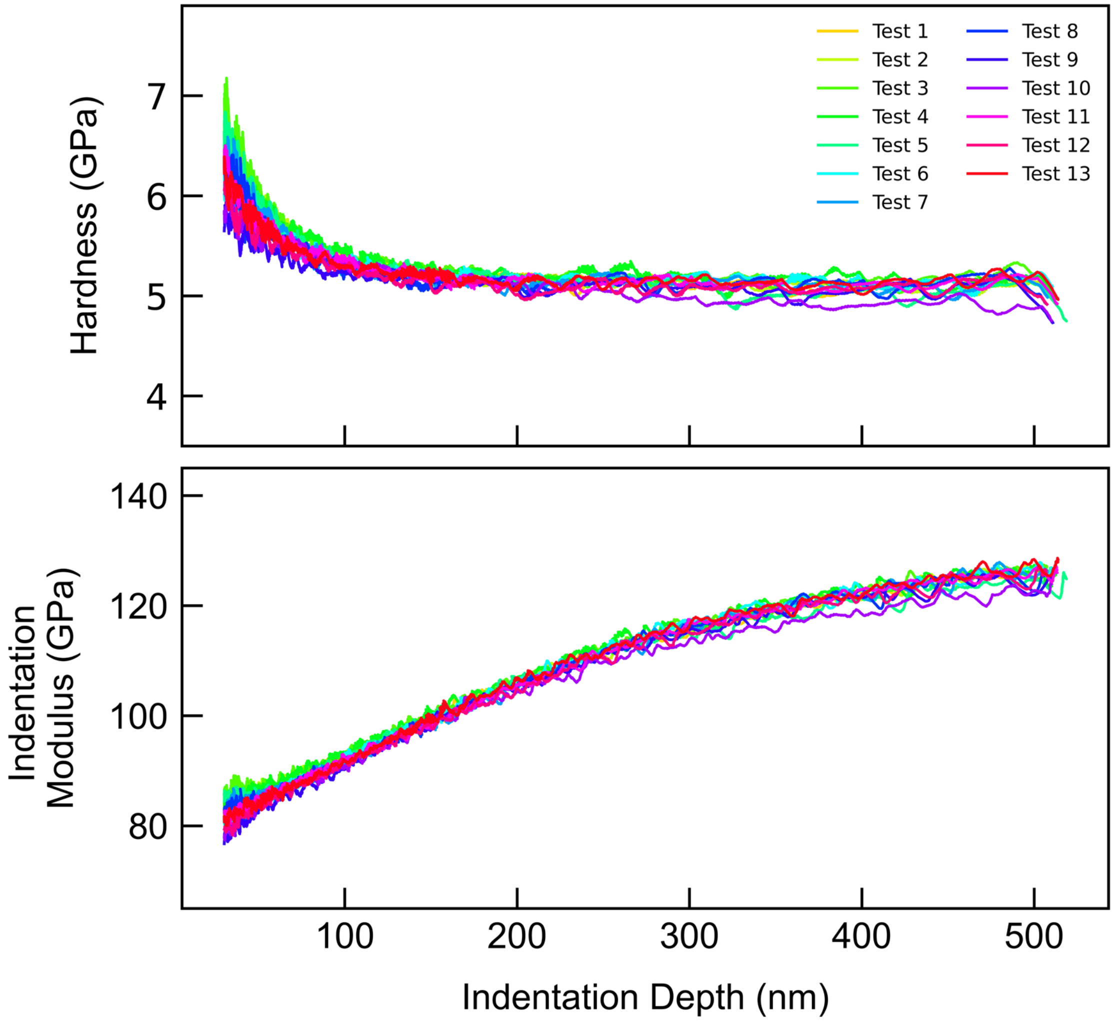

Figure A.1: *Depth resolved indentation hardness and modulus for the as deposited Al-Ni-Ce alloy.*

Appendix B: Additional *in-situ* EDS measurements

In Figure 9, we presented colorized, post-processed EDS spectral maps of the Al-Ni-Ce alloy measured at room temperature in the as-deposited condition and after heating to 325 °C. For ease of interpretation and to eliminate concerns about the effects of post-processing, the un-binned EDS maps are presented in Figures B.1 and B.2. Additional EDS maps of the precipitated (450 °C) microstructure are also displayed in Figure B.3.

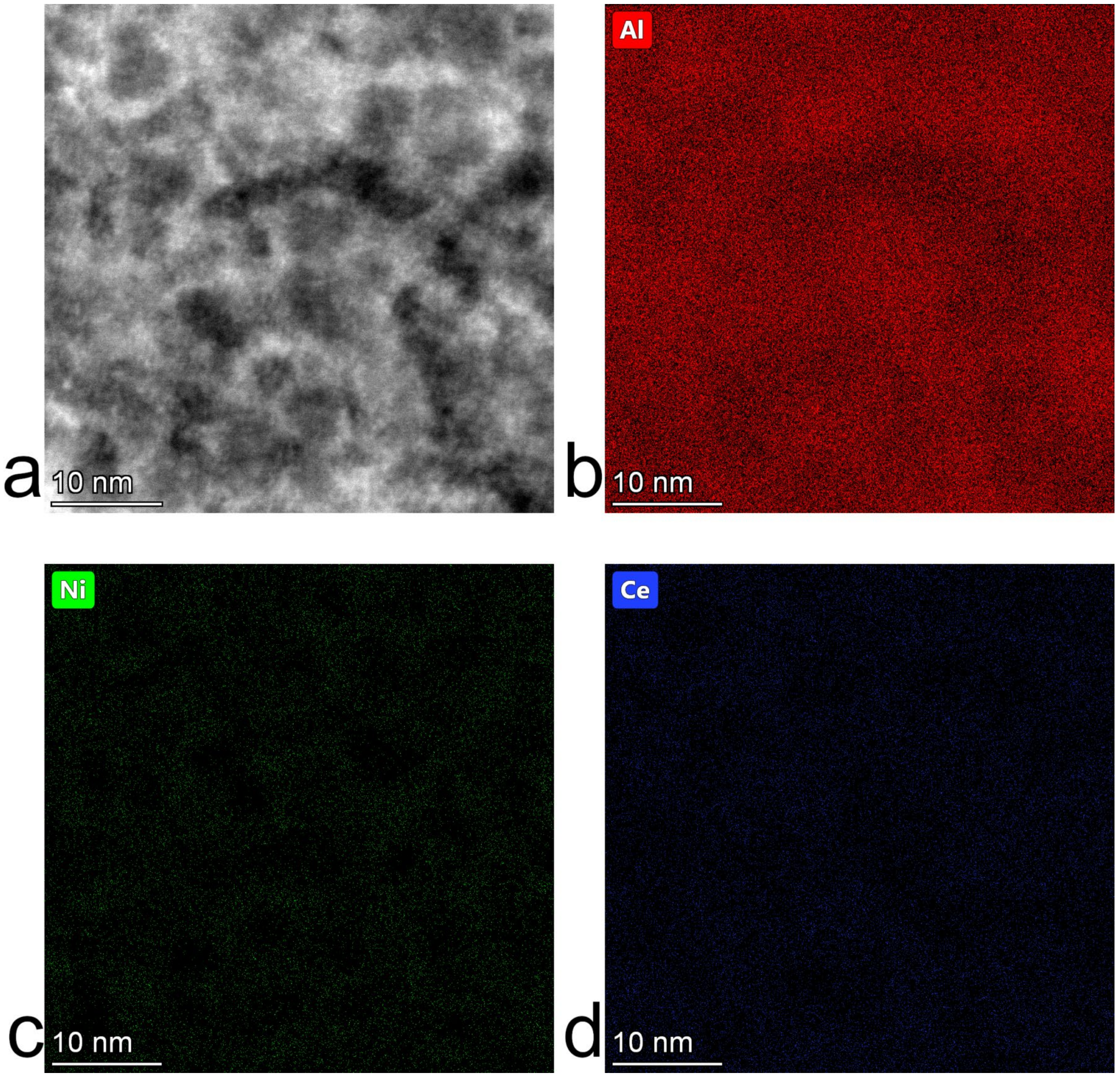

Figure B.1: *EDS map of as-deposited Al-Ni-Ce alloy.* ***a****, HAADF image. Color elemental maps of* ***b****, Al* ***c****, Ni and* ***d****, Ce.*

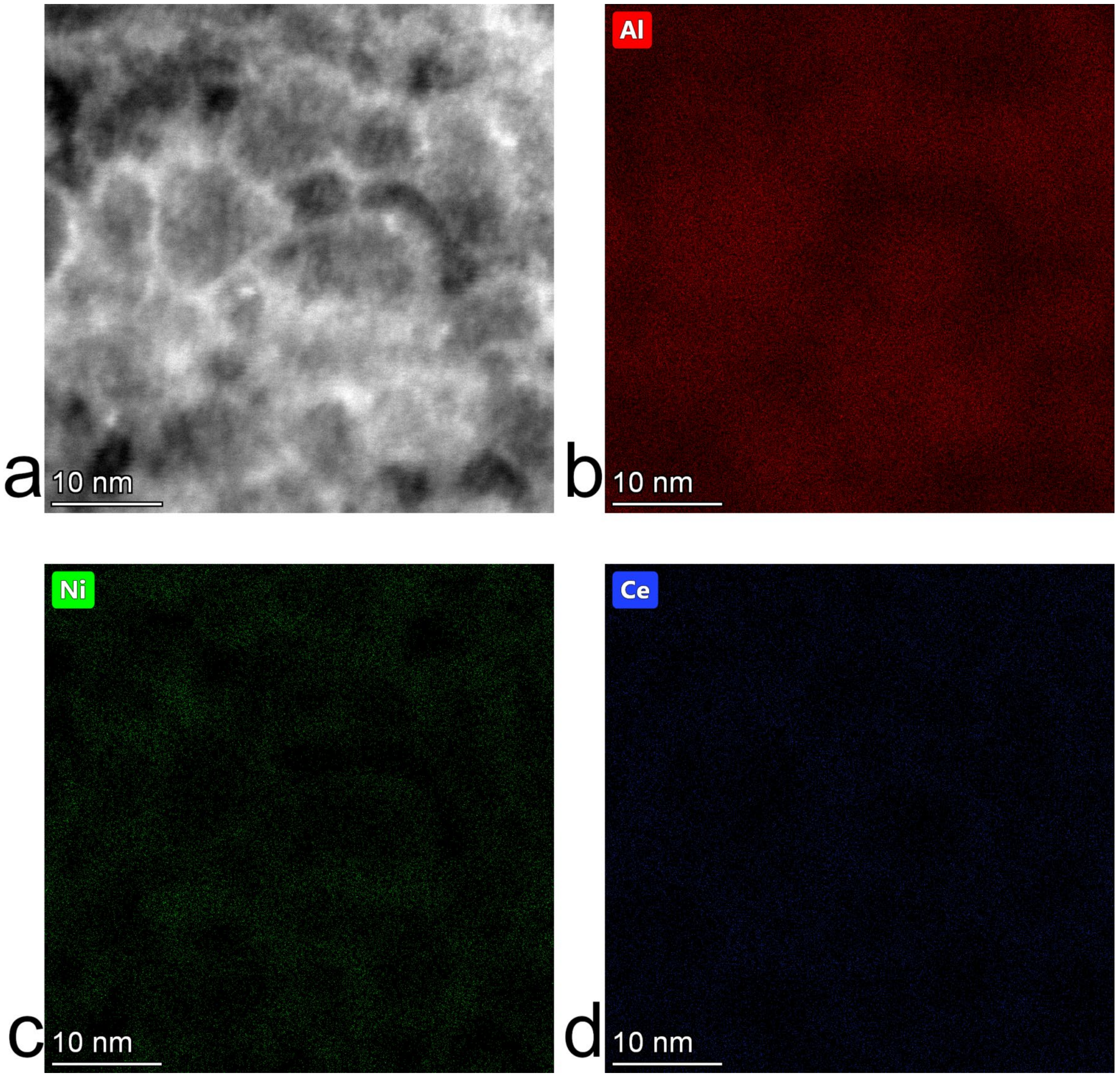

Figure B.2: *EDS map of Al-Ni-Ce alloy heated in-situ to 325 °C.* ***a****, HAADF image. Color elemental maps of* ***b****, Al* ***c****, Ni and* ***d****, Ce. Chemical redistribution of Ni and Ce to grain boundaries is qualitatively demonstrated in* ***c, d****, compared to Figure 15****c, d****.*

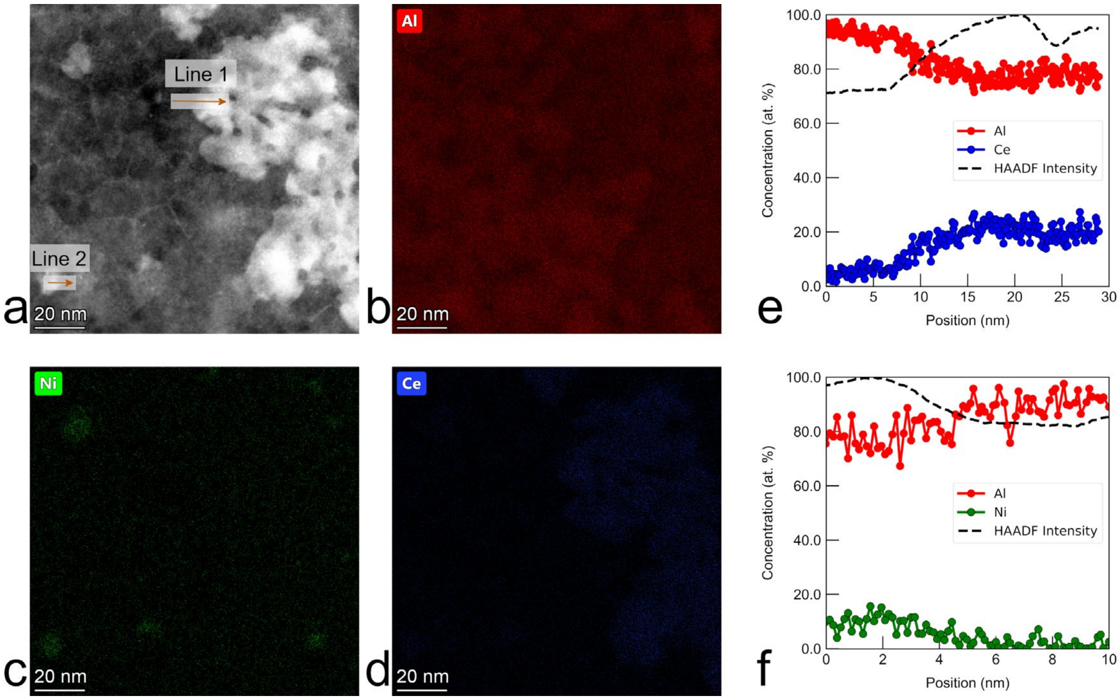

Figure B.3: *EDS map and quantification of Al-Ni-Ce alloy heated in-situ to 450 °C.* ***a****, HAADF image. Color elemental maps of* ***b****, Al* ***c****, Ni and* ***d****, Ce. Presence of Ni (*Al_3Ni*) and Ce (*$Al_{11}Ce_3$*) rich precipitates can be seen in* ***c****,* ***d****.* ***e****, Elemental line profiles of Line 1 crossing into the* $Al_{11}Ce_3$ *precipitate.* ***f****, Elemental line profiles of Line 2 beginning in an* Al_3Ni *precipitate.*